LATVIAN JOURNAL of PHYSICS and TECHNICAL SCIENCES

ISSN 0868 - 8257

(Vol. 58)

2021

CONTENTS

LATVIAN JOURNAL of PHYSICS and TECHNICAL SCIENCES

LATVIJAS FIZIKAS un TEHNISKO ZINĀTŅU ŽURNĀLS

ЛАТВИЙСКИЙ ФИЗИКО-ТЕХНИЧЕСКИЙ ЖУРНАЛ

Published six times a year since February 1964
Iznāk sešas reizes gadā kopš 1964. gada februāra
Выходит шесть раз в год с февраля 1964 года

6 (Vol. 58) • 2021

RĪGA

Language Editor: O. Ivanova
Computer Designer: I. Begicevs

INDEXED (PUBLISHED) IN

www.scopus.com
www.sciendo.com
EBSCO (Academic Search Complete, www.epnet.com), INSPEC (www.iee.org.com).
VINITI (www.viniti.ru), Begell House Inc/ (EDC, www.edata-center.com).

Issuers: Institute of Physical Energetics,
Institute of Solid State Physics, University of Latvia
Registration Certificate Number: 000700221

Editorial Contacts:
11 Krivu Street, Riga, LV - 1006
Ph.: + 371 67551732
E-mail: leo@lza.lv
www.fei-web.lv

sciendo

LATVIAN JOURNAL OF PHYSICS
AND TECHNICAL SCIENCES
2021, N 6

DOI: 10.2478/lpts-2021-0041

THE EFFECT OF THE RANGE OF A MODULATING PHASE MASK ON THE RETRIEVAL OF A COMPLEX OBJECT FROM INTENSITY MEASUREMENTS

V. Karitans[1,2]*, M. Ozolinsh[1,2], A. Lapins[3], S. Fomins[1,2]

[1]Institute of Solid State Physics, University of Latvia
8 Kengaraga Str., Riga, LV-1063, LATVIA
[2]Department of Optometry and Vision Science, University of Latvia
1 Jelgavas Str., Riga, LV-1004, LATVIA
[3]Laser Centre, University of Latvia
3 Jelgavas Str., Riga, LV-1004, LATVIA
*e-mail: Varis.Karitans@cfi.lu.lv

In many fields of science, it is often impossible to preserve the information about the phase of the electromagnetic field, and only the information about the magnitude is available. This is known as the phase problem. Various algorithms have been proposed to recover the information about phase from intensity measurements. Nowadays, iterative algorithms of phase retrieval have become popular. Many of these algorithms are based on modulating the object under study with several masks and retrieving the missing information about the phase of an object by applying mathematical optimization methods. Several of these algorithms are able to retrieve not only the phase but also the magnitude of the object under study. In this study, we investigate the effect of the range of modulation of a mask on the accuracy of the retrieved magnitude and phase map. We conclude that there is a sharp boundary of the range of modulation separating the successfully retrieved magnitude and phase maps from those retrieved unsuccessfully. A decrease in the range of modulation affects the accuracy of the retrieved magnitude and phase map differently.

Keywords: *Coherent diffractive imaging, magnitude, phase retrieval, phase problem.*

1. INTRODUCTION

Due to the extremely rapid oscillations of the electromagnetic field [1], it is often impossible to preserve the information about the phase of the field, and only the information about the magnitude is available [2]. This is widely known as the phase problem and is encountered in many fields of science. The information about the phase of the diffracted field, however, is very important to retrieve the structure of the diffracting object [3]. In order to overcome the phase problem, various algorithms of phase retrieval have been proposed. Historically, the first algorithm proposed to retrieve the phase of an object from diffraction patterns was the Gerchberg-Saxton algorithm based on alternating projections [4]. Later, Fienup modified the Gerchberg-Saxton algorithm by replacing some of the constraints in the real domain with other constraints in accordance with the measured Fourier magnitude [5]. The Fienup algorithm is itself divided into two different subversions [6]. The Gerchberg-Saxton and Fienup algorithms were followed by the transport of intensity equation (TIE) [7]. In TIE, two intensity measurements at adjacent planes are sufficient to retrieve the phase of an object. TIE has also several versions like standard TIE, higher-order TIE and Gaussian process TIE.

Today, many iterative phase retrieval algorithms have been developed. An iterative algorithm PhaseLift requires modulating the object under study by a very limited number of masks and recovers the structure of the object from coded diffraction patterns under very noisy conditions [8], [9]. The original solution to PhaseLift is based on convex optimization; however, it was later optimized using low-rank Riemannian optimization methods [10]. PhaseLift formulates phase retrieval as finding a rank-one matrix. An algorithm PhaseCut [11] may be seen as a modification of PhaseLift. PhaseCut separates phase and magnitude variables and has been shown to be more stable than PhaseLift in the presence of noise. An algorithm SR-SPAR using sparsity in a complex object domain allows achieving superresolution about a quarter wavelength [12], while an algorithm GESPAR is able to recover a sparse object from intensity measurements and repeatedly updates the support of the object to avoid getting stuck [13]. While the aforementioned algorithms have been primarily developed to solve the phase problem, as the name suggests, several of them, e.g., PhaseLift, SPAR and GESPAR are also able to retrieve the complex field, i.e., the magnitude of the object along with the phase. As already mentioned, the algorithm PhaseCut separates the phase and magnitude of the object to be recovered. Generally, the magnitude retrieved by algorithms of phase retrieval has been studied minimally [14], [15].

In this study, we simulated the retrieval of a complex object with the algorithm PhaseLift and studied its accuracy depending on the range of modulation of pure phase masks. We chose the algorithm PhaseLift for its several advantages compared to other algorithms. As already mentioned, it requires a smaller number of modulating masks compared to other algorithms. Candes and Huang [8]–[10] showed that six modulating masks were sufficient for successful phase retrieval by PhaseLift. We have shown previously that four amplitude masks generated from a single mask are sufficient for reasonable phase retrieval [16], while other algorithms require all masks being different. PhaseLift is also able to retrieve the phase of an object from

very sparse data suggesting that imaging cameras of low bit depth are sufficient for capturing diffraction patterns. As far as the authors know, the performance of PhaseLift has been studied for different types and number of modulating masks; however, the effect of the range of modulation on its performance has never been studied before.

2. METHODS

2.1. Phase Retrieval

A two-dimensional complex object to be retrieved is given by

$$x_0 \in \mathbb{C}^{n_1 x n_2}, \tag{1}$$

while its vectorized form is given by

$$\mathrm{x}_0 \in \mathbb{C}^n, \tag{2}$$

where $n = n_1 \cdot n_2$.

The discrete Fourier transform (DFT) of x_0 is given by

$$\mathfrak{I}(\mathrm{x}_0) = \mathrm{T} \cdot \mathrm{x}_0, \tag{3}$$

where the matrix T is the Kronecker product of the DFT matrix W, i.e.,

$$\mathrm{T} = \mathrm{W} \otimes \mathrm{W}. \tag{4}$$

The size of the matrix W is n_1 by n_2. Let us also suppose we have l complex random modulating masks

$$d_i \in \mathbb{C}^{n_1 x n_2}, \tag{5}$$

where $i = 1,2,...,l$.

Let us denote the vectorized form of d_i by $\mathrm{d}_i \in \mathbb{C}^n$ and point-wise multiplication by $\cdot\cdot$. The DFT of the modulated object $\mathrm{d}_i \cdot \mathrm{x}_0$ is given by

$$\mathfrak{I}(\mathrm{d}_i \cdot\cdot\, \mathrm{x}_0) = \mathrm{Z}_i \cdot \mathrm{x}_0, \tag{6}$$

where the matrix Z_i is given by an equation

$$\mathrm{Z}_i = \mathrm{T} \cdot \mathrm{Diag}(\mathrm{d}_i), \tag{7}$$

where $\mathrm{Diag}(\mathrm{d}_i)$ is an n by n matrix with the modulating waveform d_i on its main diagonal all other elements being zeros.

For the i-th mask, we have the modulus of the DFT of the modulated object in a vector b_{i_k} given by an equation

$$\mathrm{b}_{i_k} = \left| \left\langle \mathrm{z}_{i_k}, \mathrm{x}_0 \right\rangle \right|, \tag{8}$$

where z_{i_k} is the k-th row of the matrix Z_i and the index of measurement $k = 1,2,...,n$.

Let us define a matrix Z for all l masks:

$$\mathrm{Z} = \begin{pmatrix} \mathrm{Z}_1 \\ \mathrm{Z}_2 \\ \vdots \\ \mathrm{Z}_l \end{pmatrix}. \tag{9}$$

We can write

$$\mathrm{b}_p = \left| \left\langle \mathrm{z}_p, \mathrm{x}_0 \right\rangle \right|, \tag{10}$$

where z_p is the p-th row of the matrix Z and the index of measurement $p = 1,2,...,m$. Here, $m = l \cdot n = l \cdot n_1 \cdot n_2$.

If we denote a vector containing all the moduli by $\mathbf{b}$ then we can write

$$\mathbf{b} = \left| Z \cdot \mathbf{x}_0 \right|. \quad (11)$$

As only intensity, i.e., the squared modulus of the DFT or Fraunhofer diffraction pattern, is detected, we have quadratic measurements of form

$$\mathbf{b}_\bullet^2 = \mathrm{diag}(Z \cdot \mathbf{x}_0 \cdot \mathbf{x}_0^* \cdot Z^*), \quad (12)$$

where $\mathbf{b}_\bullet^2$ denotes the vector containing squared elements of the vector $\mathbf{b}$, $\mathrm{diag}(Z \cdot \mathbf{x}_0 \cdot \mathbf{x}_0^* \cdot Z^*)$ denotes the vectorial form of the matrix $Z \cdot \mathbf{x}_0 \cdot \mathbf{x}_0^* \cdot Z^*$ while the asterisk * denotes the conjugate transpose.

If we denote $\mathbf{x}_0 \cdot \mathbf{x}_0^*$ by X_0, the phase retrieval by PhaseLift can be formulated as finding a rank-one matrix [8]–[11]:

find

X_0

subject to

$\mathbf{b}_\bullet^2 = \mathrm{diag}(Z \cdot \mathbf{x}_0 \cdot \mathbf{x}_0^* \cdot Z^*)$
$X_0 \succ= 0$
$\mathrm{rank}(X_0) = 1$

Here, X_0 is the rank-one solution and factorizing it in the form $\mathbf{x}_0 \cdot \mathbf{x}_0^*$ yields the solution to the phase retrieval problem. The rank minimization problem, however, is NP hard and in convex programming can be relaxed to trace minimization:

min

$\mathrm{trace}(X_0)$

subject to

$\mathbf{b}_\bullet^2 = \mathrm{diag}(Z \cdot \mathbf{x}_0 \cdot \mathbf{x}_0^* \cdot Z^*)$
$X_0 \succ= 0$

Huang suggested using an alternate cost function due to the complexity associated with convex programming [10]. It is known that if the rank of X_0 is p, then there is $Y_p \in \mathbb{C}^{nxp}$ satisfying $Y_p \cdot Y_p^* = X_0$. Then the following cost function can be used:

$$f_r\left([Y_r]\right) = \frac{\left\| \mathbf{b}_\bullet^2 - \mathrm{diag}(Z \cdot Y_r \cdot Y_r^* \cdot Z^*) \right\|_2^2}{\left\| \mathbf{b}_\bullet^2 \right\|_2^2} \quad (13)$$

PhaseLift optimizes the cost function in each iteration using one of several low-rank Riemannian optimization methods [10]. The algorithm was stopped when the norm of the gradient of the cost function fell below 10^{-5}.

2.2. Simulations

Complex objects of unity large magnitude maps and distorted phase maps were used as test objects in the simulations (see Fig. 1 left). The phase maps of the objects were scaled versions of each other. One of the objects was selected as the original object, while the phase maps of other objects were obtained by multiplying the phase map of the original object with a scaling factor s taking values 0.5, 1.5, 2.0., and 2.5. In order to generate the phase map of the original object, random Zernike coefficients in the range from -1 μm to 1 μm up to the 6th order were generated. The units of phase distortions were radians. The size of the objects were 256 by 256 pixels.

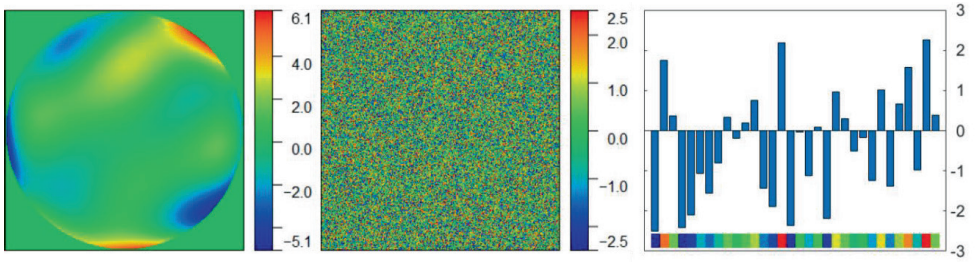

Fig. 1. Left – one of the objects used in the simulations. The scale on the right side is given in radians. Middle – one of the phase masks with the range of modulation = 0.8. The scale on the right side is given in radians. Right – the surface profile of a cut-out of the phase mask. The length of the cut-out is 16 pixels.

The root-mean-square error of the phase map of an object $RMSE_{po}$ was calculated according to an equation

$$RMSE_{po} = \sqrt{\frac{\sum_{i=1}^{n} (\overline{\varphi_0} - \varphi_{0i})^2}{n}}, \quad (14)$$

where $\overline{\varphi_0}$ is the average value of all data points of a phase map φ_0, φ_{0i} is the value of the i-th data point, and n is the number of data points.

In order to assess the quality of the retrieved magnitude map A_r, the root-mean-square error of the residual magnitude map of an object $RMSE_{mres}$ was calculated according to an equation

$$RMSE_{mres} = \sqrt{\frac{\sum_{i=1}^{n} \left(\left(\overline{A_0 - A_r} \right) - \left(A_0 - A_r \right)_i \right)^2}{n}}, \quad (15)$$

where $\overline{A_0 - A_r}$ is the average value of all data points of the residual magnitude map $A_0 - A_r$, $\left(A_0 - A_r\right)_i$ is the value of the i-th data point, and n is the number of data points.

In order to assess the quality of the retrieved phase map, the root-mean-square error of the residual phase map of an object $RMSE_{pres}$ was calculated according to an equation

$$RMSE_{pres} = \sqrt{\frac{\sum_{i=1}^{n} \left(\left(\overline{\varphi_0 - \varphi_r} \right) - \left(\varphi_0 - \varphi_r \right)_i \right)^2}{n}}, \quad (16)$$

where $\overline{\varphi_0 - \varphi_r}$ is the average value of all data points of the residual phase map $\varphi_0 - \varphi_r$, $\left(\varphi_0 - \varphi_r\right)_i$ is the value of the i-th data point, and n is the number of data points.

In order to compare the $RMSE_{pres}$ among objects with different $RMSE_{po}$, the $RMSE_{pres}$ was divided by the respective $RMSE_{po}$.

The masks used to modulate the object were of the same size as the object. The masks were random pure phase masks modulating the phase of the object at each point by a random value within a certain range (see Fig. 1 right). The inset shown on the right side of Fig. 1 is a region of the phase mask contained within the white square. Here, we introduce the range of modulation of a mask denoted by M and defined as

$$M = \frac{\varphi_{\max} - \varphi_{\min}}{2 \cdot \pi}, \quad (17)$$

where $\varphi_{\max}$ and $\varphi_{\min}$ are the maximum and minimum value of the phase mask, respectively, within the range from -π to +π.

The range of modulation M varied between 0.1 and 0.8 in steps of 0.1. The selected range of modulation was based on

a spatial light modulator (SLM) available in our laboratory guaranteeing that the range of phase modulation M as the results of simulations indicate the achievable accuracy of the retrieved magnitude and phase maps of an object. The size of a pixel of the SLM is 8 μm so that an object and mask of size 256 by 256 pixels correspond to the linear size 2048 by 2048 μm. The maximum phase shift that can be introduced by the SLM is 2.9·π radians at the wavelength of a He-Ne laser (λ = 0.6328 μm corresponding to 2·π radians). The peak-to-valley value of the original object was about 11.2 radians corresponding to about 1.1 μm at the wavelength of a He-Ne laser.

3. RESULTS

Figure 2 shows the retrieved magnitude and phase maps of the object with the scaling factor $s = 2$ for all ranges of modulation M. The range of modulation M increases from left to right and from top to bottom. It can be easily noticed that the range of modulation M of at least 60 % of a full wave is required for a successful retrieval of the magnitude map of the selected object. A sharp boundary separating successfully retrieved magnitude maps from those retrieved unsuccessfully was characteristic of all objects. The values of the magnitude maps are shown in arbitrary units and have been normalized so that the maximum value equals unity.

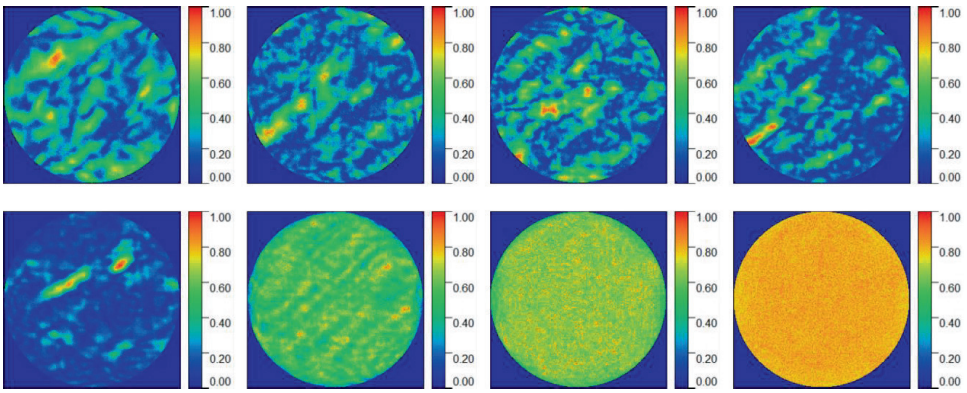

Fig. 2. The retrieved magnitude maps of the object with the scaling factor $s = 2$ for all ranges of modulation M changing from 0.1 to 0.8 in steps of 0.1. The range of modulation M increases from left to right and from top to bottom. One can notice the sharp boundary separating successfully retrieved magnitude maps from those retrieved unsuccessfully.

Figure 3 shows the retrieved phase maps of the same object with the scaling factor $s = 2$ for all ranges of modulation M. The retrieved phase maps were wrapped within the range from -π to +π and had to be unwrapped using an algorithm freely available on the Internet. The retrieved phase map is also comparable to the original one starting from the same range of modulation M, i.e., 60 %. Below this level, there is no similarity between the retrieved phase map and the object. Generally, the minimum values of the range of modulation M for successful retrieval of the magnitude and phase map are always equal given one and the same object. The units of phase maps are given in radians.

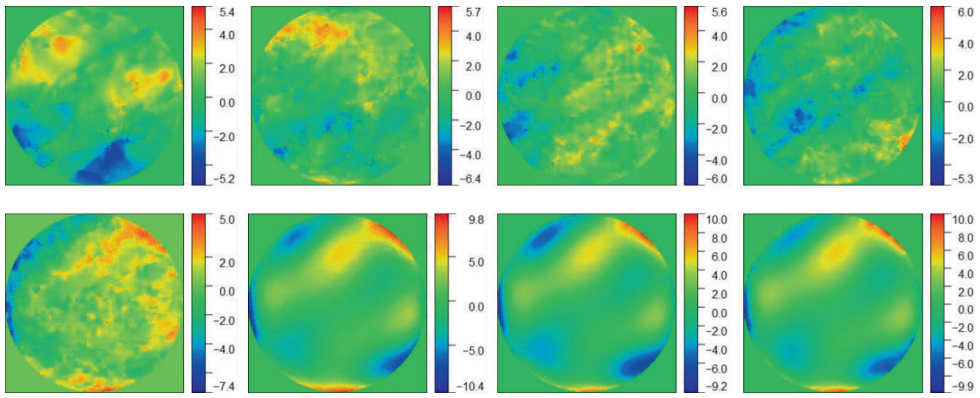

Fig. 3. The retrieved phase maps of the object with the scaling factor $s = 2$ for all ranges of modulation M changing from 0.1 to 0.8 in steps of 0.1. The range of modulation M increases from left to right and from top to bottom. One can notice the sharp boundary separating successfully retrieved phase maps from those retrieved unsuccessfully.

Figure 4 shows the $RMSE_{mres}$ (left) and the normalized $RMSE_{pres}$ (right) for all ranges of modulation M. The error bars are standard errors calculated from the results of five simulations. The labels top right show the $RMSE_{po}$ of the objects. The $RMSE_{pres}$ was normalized by dividing it with the corresponding $RMSE_{po}$. It can be easily noticed that the $RMSE_{mres}$ grows for all objects as the range of modulation M is reduced while three distinct regions of the $RMSE_{pres}$ can be noted. For the largest range of modulation M, i.e., 0.8 of a full wave, the $RMSE_{pres}$ of all objects is low except the object having the smallest $RMSE_{po}$. Starting from a certain value of the range of modulation M, the $RMSE_{pres}$ starts to increase rapidly as the range of modulation M is decreased. The exact range of modulation M at which the $RMSE_{pres}$ starts to grow rapidly depends on the $RMSE_{po}$. It should also be noted that the highest $RMSE_{pres}$ also depends on the $RMSE_{po}$, i.e., the $RMSE_{pres}$ was higher for objects having small $RMSE_{po}$. As the range of modulation M is further reduced, the $RMSE_{pres}$ of objects having small $RMSE_{po}$ remained constant while the $RMSE_{pres}$ of objects having large $RMSE_{po}$ started to fall reaching the level of objects having small $RMSE_{po}$.

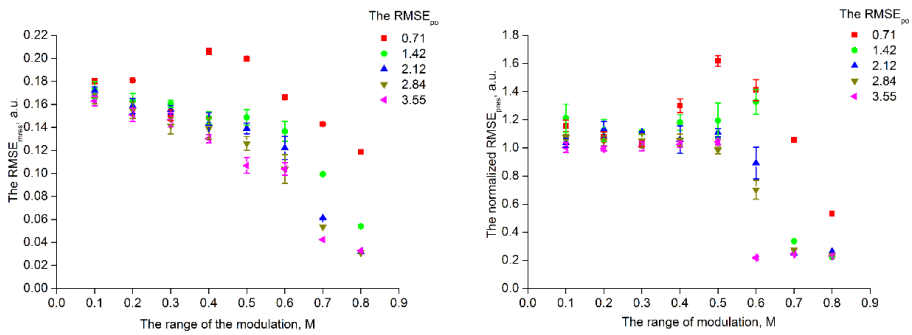

Fig. 4. Dependence of the $RMSE_{mres}$ (left) and $RMSE_{pres}$ (right) on the range of modulation M. Generally, the growth of the $RMSE_{mres}$ is similar for all objects except the object with the smallest $RMSE_{po}$. The $RMSE_{pres}$ is always low for large ranges of modulation M irrespective of $RMSE_{po}$. For medium ranges of modulation M, the $RMSE_{pres}$ strongly depends on the $RMSE_{po}$ while for low small ranges of modulation M the $RMSE_{pres}$ is approximately constant and does not vary considerably with the $RMSE_{po}$.

4. DISCUSSION AND CONCLUSIONS

The results suggest that the retrieval of the magnitude and phase of an object is compromised differently as the range of modulation is reduced. Differences between the changes in the $RMSE_{mres}$ and $RMSE_{pres}$ along with the changes in the range of modulation M may be explained by separating the magnitude and phase of an object and analysing the spatial spectrum of both components.

The magnitude map being completely flat contains predominantly low spatial frequencies, and hence the intensity of high spatial frequencies strongly depends on the range of modulation M. Due to zeroing the high spatial frequencies because of the low bit depth, the amount of information carried by the high spatial frequencies decreases and the $RMSE_{mres}$ increases as the range of modulation M decreases. For all objects, except the object with the smallest $RMSE_{po}$, the effect of the $RMSE_{po}$ on the $RMSE_{mres}$ seems negligible.

The analysis of the effect of the range of modulation M on the $RMSE_{pres}$ is more complicated. In the region, where the range of modulation M is low, high spatial frequencies are of low intensity irrespective of the $RMSE_{po}$ and are forced to zero due to the low bit depth. The bright central part occupies about the same region of the diffraction pattern irrespective of the $RMSE_{po}$, and therefore the normalized $RMSE_{pres}$ is approximately constant. In the region, where the range of modulation M is large, high spatial frequencies are intense for all objects despite the low bit depth ensuring favourable conditions for the algorithm to converge to a solution.

One can also note that smaller ranges of modulation M are required for objects of large $RMSE_{po}$ compared to objects of smaller $RMSE_{po}$. The middle region is a transition between the two extremes where zeroing the high spatial frequencies depends both on the M and the $RMSE_{po}$. If the $RMSE_{po}$ is small, the high spatial frequencies are still forced to zero because of the low bit depth despite that the range of modulation M is moderate; however, for objects with higher $RMSE_{po}$ high spatial frequencies are non-zero. Particularly large $RMSE_{pres}$ of the object with the smallest $RMSE_{po}$ suggests that the probability of unsuccessful phase retrieval from very sparse intensity measurements increases as the range of modulation M increases given that the sparsity of the intensity measurements remains the same. To summarise, the effect of the range of modulation M dominates when reaching the extreme values while at moderate levels of the range of modulation M the contents of spatial frequencies of the object dictate the $RMSE_{pres}$.

Finally, we conclude that increasing the bit depth of intensity measurements may lower the minimum the range of modulation M sufficient for successful retrieval of a complex object. It can also be expected that the probability of retrieving an object with small $RMSE_{po}$ increases as the bit depth is increased given that the range of modulation M remains the same. Objects having particularly large $RMSE_{po}$ may even be retrieved from diffraction patterns of very low bit depth.

Ability to retrieve phase maps having large $RMSE_{po}$ from very sparse intensity measurements is very important in astronomy where imaging the celestial objects is compromised by very turbulent atmospheric layers [17]. Studying the effect of bit depth on the quality of phase and mag-

nitude retrieval constitutes a wide scope of research, and we plan to address this question in future. It can also be expected that oversampling the diffraction patterns may lower the requirements of the minimum necessary range of modulation M .

ACKNOWLEDGEMENTS

The authors have been supported by the postdoctoral project (1.1.1.2/16/I/001, 1.1.1.2/VIAA/1/16/199), the CAMART2 project (grant agreement ID 739508), the Latvian Investment and Development Agency (LIDA) project (KC-PI-2017/105), and the grant for the Latvian State Emeritus Scientists.

REFERENCES

1. Shechtman, Y., Eldar, Y.C., Cohen, O., Chapman, H. N., Miao, J., & Segev, M. (2015). Phase Retrieval with Application to Optical Imaging. *IEEE Signal Processing Magazine*, *32* (3), 87–109. DOI: 10.1109/MSP.2014.2352673
2. Zuo, C., Li, J., Sun, J., Fan, Y., Zhang, J., Lu, L., ... & Chen, Q. (2020). Transport of Intensity Equation: A Tutorial. *Optics and Lasers in Engineering*, *135*, 106187. DOI: 10.1016/j.optlaseng.2020.106187
3. Tao, S., He. C., Hao, X., Kuang, C., & Liu, X. (2021). Principles of Different X-ray Phase-Contrast Imaging: A Review. *Applied Sciences (Switzerland)*, *11* (7), 2971. DOI: 10.3390/app11072971
4. Gerchberg, R. W., & Saxton, W.O. (1972). Practical Algorithm for the Determination of Phase from Image and Diffraction Plane Pictures. *Optik (Stuttgart)*, *35* (2), 237–250.
5. Fienup, J. R. (1982). Phase Retrieval Algorithms: A Comparison. *Applied Optics*, *21* (15), 2758–2768. DOI: 10.1364/AO.21.002758
6. Latychevskaia, T. (2018). Iterative Phase Retrieval in Coherent Diffractive Imaging: Practical Issues. *Applied Optics*, *57* (25), 7187–7197. DOI: 10.1364/AO.57.007187
7. Huang, L., Zuo, C., Idir, M., Qu, W., & Asundi, A. (2015). Phase retrieval in arbitrarily shaped aperture with the transport-of-intensity equation. In *SPIE/IS&T Electronic Imaging* (94010B), 8–12 February 2015, San Francisco, California, United States: SPIE Digital Library. DOI: 10.1117/12.2087754
8. Candès, E. J., Eldar, Y. C., Strohmer, T., & Voroninski, V. (2013). Phase Retrieval via Matrix Completion. *SIAM Journal on Imaging Sciences*, *6* (1), 199–225. DOI: 10.1137/110848074
9. Candès, E. J., Li, X., & Soltanolkotabi, M. (2015). Phase Retrieval from Coded Diffraction Patterns. *Applied and Computational Harmonic Analysis*, *39* (2), 277–299. DOI: 10.1016/j.acha.2014.09.004
10. Huang, W., Gallivan, K. A., & Zhang, X. (2017). Solving PhaseLift by Low-rank Riemannian Optimization Methods for Complex Semidefinite Constraints. *SIAM Journal on Scientific Computing*, *39* (5), B840–B859. DOI: 10.1137/16M1072838
11. Waldspurger, I., d'Aspremont, A., & Mallat, S. (2015) Phase Recovery, MaxCut and Complex Semidefinite Programming. *Mathematical Programming*, *149* (1–2), 47–81. DOI: 10.1007/s10107-013-0738-9
12. Katkovnik, V., & Egiazarian, K. (2017). Sparse Superresolution Phase Retrieval from Phase-coded Noisy Intensity Patterns. *Optical Engineering*, *56* (9), 094103. DOI: 10.1117/1.OE.56.9.094103
13. Shechtman, Y., Beck, A., & Eldar, Y. C. (2014). GESPAR: Efficient Phase Retrieval of Sparse Signals. *IEEE Transactions on Signal Processing*, *62* (4), 928–938. DOI: 10.1109/TSP.2013.2297687

14. Kumar Singh, R., Vinu, R. V., & Sharma M., A. (2014). Recovery of Complex Valued Objects from Two-point Intensity Correlation Measurement. *Applied Physics Letters*, *104* (11), 111108. DOI: 10.1063/1.4869123
15. Knapp, J., Paulus, A., Komprobst, J., Siart, U., & Eibert, T. F. (2021). Multifrequency Phase Retrieval for Antenna Measurements. *IEEE Transactions on Antennas and Propagation*, *69* (1), 488-501. DOI: 10.1109/TAP.2020.3008648
16. Karitans, V., Nitiss, E., Tokmakovs, A., Ozolinsh, M., & Logina, S. (2019). Optical Phase Retrieval Using Four Rotated Versions of a Single Binary Amplitude Modulating Mask. *Journal of Astronomical Telescopes, Instruments, and Systems*, *5* (3), 039004. DOI: 10.1117/1.JATIS.5.3.039004
17. Burke, D., Devaney, N., Christof, J., & Hartung, M. (2010). Application of wavelength diversity for astronomical adaptive optics imaging. In *SPIE Astronomical Telescopes + Instrumentation*, (77365U), 27 June–2 July 2010, San Diego, California, United States: SPIE Digital Library. DOI: 10.1117/12.856953

sciendo

LATVIAN JOURNAL OF PHYSICS
AND TECHNICAL SCIENCES
2021, N 6

DOI: 10.2478/lpts-2021-0042

INFLUENCE OF "PRODUCTIVE" IMPURITIES (Cd, Na, O) ON THE PROPERTIES OF THE Cu_2ZnSnS_4 ABSORBER OF MODEL SOLAR CELLS

D. Sergeyev[1, 2*], N. Zhanturina[1*], A. Aizharikov[2], A.I. Popov[3*]

[1] K. Zhubanov Aktobe Regional University, Aktobe, KAZAKHSTAN
[2] T. Begeldinov Aktobe Aviation Institute, Aktobe, KAZAKHSTAN
[3] Institute of Solid State Physics, University of Latvia,
8 Kengaraga Str., Riga, LATVIA
*e-mail: serdau@mail.ru, nzhanturina@mail.ru, popov@latnet.lv

The study focuses on the optical properties of the CZTS multicomponent semiconductor absorber with 3 % "production" impurities of Cd, Na, O within the framework of the density functional theory using the generalized gradient approximation and the SCAPS program, as well as investigates their influence on the performance and efficiency of CZTS-solar cells. The results showed that the introduction of Cd, Na, O impurities would lead to a decrease in the intensity of the absorption bands at 2.06 eV and 2.55 eV. The density of states CZTS: (Cd, Na, O) was determined from first principles, and it was revealed that impurities of Cd and O atoms would lead to a decrease in the band gap (to 0.9 eV and 0.79 eV), and an increase in Na impurity absorption (1.2 eV). It was also found that a decrease in the band gap led to a decrease in the open circuit voltage, and it was also shown that "industrial" impurities led to a decrease in the efficiency of energy conversion of solar cells to 2.34 %.

Keywords: *Cu_2ZnSnS_4 (CZTS), density of states, JV-characteristics, optical absorption coefficient, SCAPS, solar cell.*

1. INTRODUCTION

Currently, one of the most emerging problems is the lack of energy resources and environmental pollution. For a comprehensive solution of these environmental tasks, it is of interest to use renewable energy sources, as well as to increase their share of consumption. Promising areas of alternative energy are the use of solar energy, the movement of air masses, ebb and flow, sea currents and others. To convert the listed types of energy into electrical energy, energy converters are needed, as well as efficient operation of power supply, energy storage devices are required. The solution to these problems will make it possible to create highly efficient, economical and environmentally-friendly power supply systems.

Note that various options have already been proposed and successfully developed for energy converters, such as solar batteries [1]–[3], wind generators [4], [5], geothermal converters [6], as well as for different energy storage devices, such as a superconducting inductive storage [7]. To improve the performance of these systems, new properties of solar radiation absorbers [8]–[10], quasi-two-dimensional materials [11]–[13], superconductors [14]–[16] and others are being searched.

Solar energy is the most economical and efficient among all the listed renewable energy sources. Therefore, in recent years, active work has been carried out to introduce alternative sources of power supply to various objects of special equipment with autonomous electricity based on photovoltaic modules using solar energy. To improve the output energy characteristics of such modules, the electronic properties of nanomaterials [17]–[20], due to quantum-size effects, are being intensively studied. The application of the quantum properties of quasiparticles can lead to a significant improvement in the basic parameters of photoelectronic devices.

It is impossible to develop new types of solar cells without understanding the ongoing physical and chemical processes when converting solar energy into electrical energy. Currently, work is underway to study thin-film solar cells based on Cu (In, Ga) (S, Se)2 (CIGS) [21]–[23]. This is due to the fact that they have high absorption coefficients and are relatively cheap [24]. However, despite the above advantages, thin-film solar cells based on CIGS are inferior to their counterparts in terms of efficiency and radiation resistance, and the elements In and Ga included in CIGS are highly toxic substances. In order to avoid the expensive disposal of such toxic elements for the creation of thin-film solar cells, the photovoltaic properties of environmentally-friendly materials are being intensively studied. By replacing highly toxic elements In, Ga, respectively, with non-toxic elements Zn, Sn, a multicomponent semiconductor compound Cu2ZnSn (S, Se)4 (CZTS) was obtained [25]. The unit cell of the CZTS structure is shown in Fig. 1.

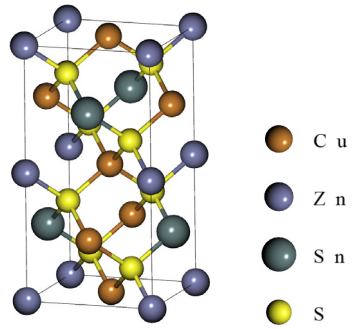

Fig. 1. Unit cell structure of CZTS.

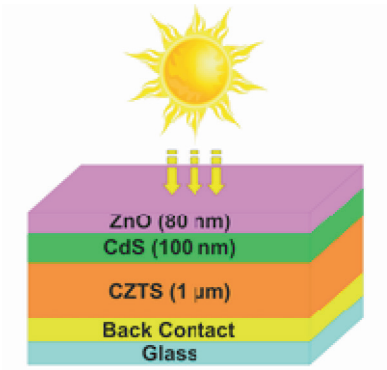

Fig. 2. Multicomponent solar cell model based on CZTS.

Thin-film solar cells based on $Cu_2ZnSn(S,Se)_4$ are a layered structure of the type ZnO/CdS/CZTS, i-ZnO/ZnS/CZTS, etc., see, for example, Fig. 2. Such layered and multicomponent structures are very complex and during production the absorber of the CZTS solar cell is contaminated with various impurities, for example, cadmium from the adjacent layer of CdS, Na from glass, as well as oxygen, nitrogen and hydrogen atoms penetrating from the air; therefore, we will call such impurities "production". Despite the low concentration of industrial impurities, they affect the optical characteristics of the absorber, which is important to take into account when developing high-performance solar cells.

In this paper, within the framework of the density functional theory using the generalized gradient approximation (DFT-GGA), the optical properties of the CZTS absorber with 3% Cd, Na and O impurities are determined, and the effects of these impurities are estimated using the SCAPS program (a Solar Cell Capacitance Simulator) on the electrical transport properties of a solar cell by the example of the structure i-ZnO/CdS/CZTS/glass.

2. SIMULATION MODEL AND METHODS

The procedure for optimizing the CZTS geometry and describing the interatomic interaction was carried out within the framework of the density functional theory (DFT); the generalized gradient approximation GGA-PBE was used as the exchange-correlation functional [26]. When optimizing the structures, the atomic configuration parameters were relaxed until the forces on all atoms became less than a predetermined threshold value of 0.05 eV/Å.

Computer simulation of the optical characteristics of CZTS, CZTS: Cd, CZTS: Na, CZTS: O was carried out within the DFT-GGA using the Kubo-Greenwood equation, which determined their dielectric susceptibility:

$$\chi_{ij}(\omega) = -\frac{e^2\hbar^4}{m_e^2\varepsilon_0 V\omega^2}\sum_{nm}\frac{f(E_m)-f(E_n)}{E_{nm}-\hbar\omega-i\hbar\Gamma}\pi^i_{nm}\pi^j_{mn}, \quad (1)$$

where π^i_{nm} is i-component of the dipole matrix element between state n and m; V – the volume; Γ – the broadening; e – the charge of the electron; $\hbar$ – Planck's constant; E – energy; $f(E)$ – the Fermi distribution function of quasiparticle energy; ε_0 – dielectric constant of vacuum; ω – frequency; m_e – electron mass.

From Eq. (1), the dependence of the dielectric constant on frequency (on energy) is determined:

$$\varepsilon(\omega) = 1 + \chi(\omega). \quad (2)$$

Using the imaginary and real parts of the dielectric constant (2), we find the extinction coefficient:

$$k(\omega) = \sqrt{\frac{\sqrt{\mathrm{Re}(\varepsilon)^2 + \mathrm{Im}(\varepsilon)^2} - \mathrm{Re}(\varepsilon)}{2}}. \quad (3)$$

From (3) optical absorption coefficient is determined:

$$\alpha = 2\frac{\omega}{c}k. \quad (4)$$

Simulation of optical properties of CZTS is done using program Atomistix ToolKit with Virtual NanoLab [27].

To determine the density of state of CZTS, we first calculate its local density of states (LDOS):

$$D(\varepsilon, r) = \sum_{ij} \rho_{ij}(\varepsilon)\phi_i(r)\phi_j(r), \quad (5)$$

where $\rho(\varepsilon) = \rho^L(\varepsilon) + \rho^R(\varepsilon)$, $\phi(r)$ – base orbitals. The density of states CZTS is obtained by integrating the LDOS over the entire space:

$$D(\varepsilon) = \int drD(\varepsilon) = \sum_{ij} \rho_{ij}(\varepsilon) S_{ij}, \quad (6)$$

where $S_{ij} = \int \phi_i(r)\phi_j(r)dr$ – the overlap matrix.

In this paper, the assessment of the influence of Cd, Na, O impurities on the output parameters of solar cells based on the CZTS absorber was carried out using the SCAPS program developed by the Department of Electronics and Information Systems (ELIS) of the University of Ghent [28]–[31]. Using the SCAPS program, the output energy parameters of multicomponent solar cells CZTS / CdS / i-ZnO / glass, CZTS: Cd / CdS / i-ZnO / glass, CZTS: Na / CdS / i-ZnO / glass, CZTS: O / CdS / i-ZnO / glass were simulated.

The calculation of the photovoltaic parameters of solar cells based on CZTS was carried out by numerically solving the basic equations of the semiconductor (Poisson's equation, which relates the electrostatic potential to the total charge density):

$$\frac{\partial}{\partial x} = \left(\varepsilon_0 \varepsilon_r \frac{\partial \psi}{\partial x}\right) = -e\left(p - n - N_D^+ - N_A^- + \frac{\rho_{def}}{e}\right), \quad (7)$$

where ψ – electrostatic potential; ε_r – semiconductor dielectric constant; N_D^+ – ionized donor concentration; N_A^- – ionized acceptor concentration; p – free hole concentration; n – free electron concentration; ρ_{def} – defect charge density.

Drift and diffusion mechanisms of charge carrier transport in semiconductors are described, respectively, by the following equations:

$$J_n = D_n \frac{dn}{dx} + \mu_n n \frac{d\phi}{dx}, \quad (8.1)$$

$$J_p = D_p \frac{dp}{dx} + \mu_p p \frac{d\phi}{dx}, \quad (8.2)$$

where J_n and J_p – current density of electrons and holes; D_n and D_p – diffusion coefficients of electrons and holes; ϕ – electric field; μ_n and μ_p – mobility of electrons and holes, respectively.

The external quantum efficiency of a model solar cell is determined by the formula:

$$EQE = \frac{J_{ph}(\lambda)}{eF(\lambda)}, \quad (9)$$

where $J_{ph}(\lambda)$ – total photogenerated current density; $F(\lambda)$ – solar stream. Solar radiation AM 1.5 with a power density of 100 mW/cm^2 is used as a source of sunlight. Note that the SCAPS software calculates the photovoltaic parameters taking into account the Shockley-Reed-Hall recombination statistics.

The basic SCAPS equations are described in detail in [28]–[31].

3. RESULTS AND DISCUSSION

Figure 3 shows the results of calculating the optical characteristics of CZTS, CZTS: Cd, CZTS: Na, CZTS: O. As can be seen, a significant contribution to the extinction coefficient is made by the imaginary part of the dielectric constant (see Eq. (3)). CZTS absorbs radiation in a wide energy range of ~ 1.6–3 eV, forming 2 absorption bands at energies of 2.06 eV and 2.55 eV. Note that one more absorption band outside the considered interval appears at 1.2 eV.

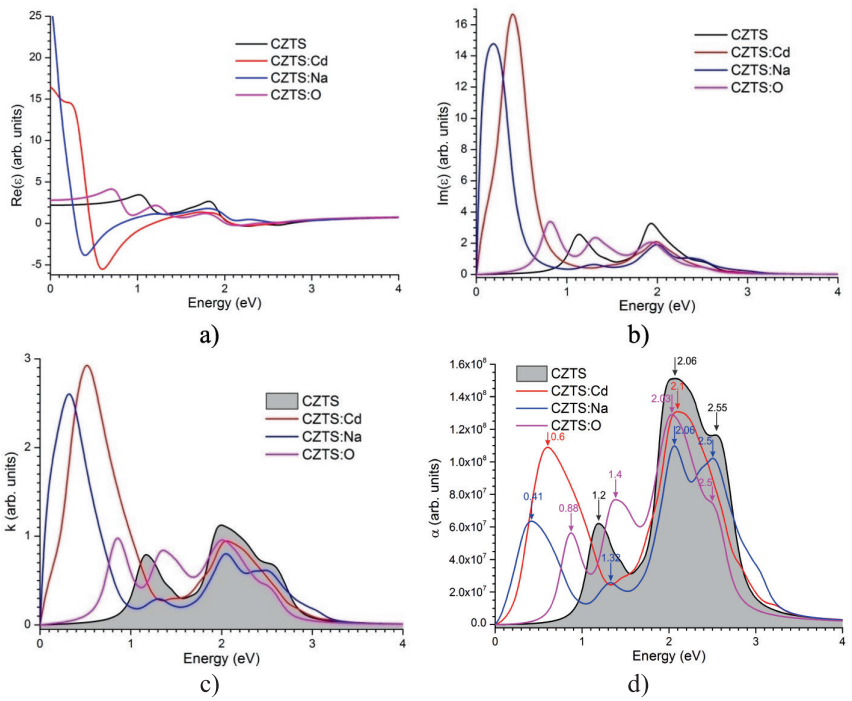

Fig. 3. Optical characteristics of the absorber CZTS:
a) real parts of the dielectric constant Re(ε);
b) complex parts of the dielectric constant Im(ε);
c) k is the extinction coefficient;
d) α – the optical absorption coefficient.

The introduction of 3 % Cd impurities, which replace mainly Zn atoms in the CZTS crystal lattice, will lead to a decrease in the intensity of the absorption spectrum at 2.1 eV; however, at 0.6 eV, a new band appears, and the band at ~ 1.2 eV disappears. An impurity of Na will also lead to a decrease in the intensities of the absorption band at 2.06 eV and 2.5 eV. The absorption band at 1.2 eV shifts to the high-energy side of 1.32 eV, and a new band appears at 0.41 eV. An impurity of an oxygen atom substituting a sulfur atom in the crystal lattice will lead, as in the case of other impurities, to a decrease in the intensity of the main absorption bands and their insignificant energy displacement of 2.03 eV and 2.5 eV. Moreover, in the low-energy region (at 0.88 eV and 1.4 eV), new absorption bands appear.

Figure 4 shows the results of calculating the density of states (DOS) CZTS, CZTS: Cd, CZTS:Na, CZTS:O. As can be seen, 3 % impurity of Cd and O atoms will lead to a decrease in the band gap from 1.1 eV to 0.9 eV and 0.79 eV, respectively, and the same concentration of Na impurity increases the band gap to 1.2 eV. Small changes in the CZTS bandgap affect other energy parameters of solar cells based on them.

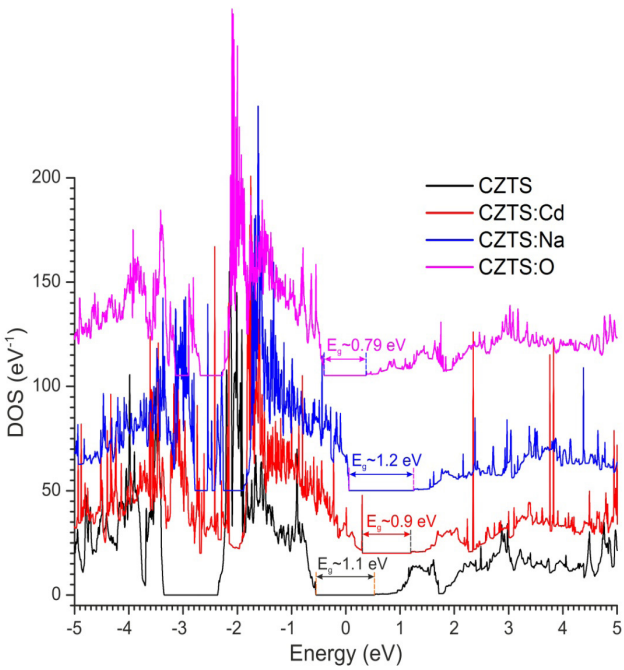

Fig. 4. Density of states of CZTS crystals.

Table 1 shows the main energy output parameters of a CZTS-based solar cell: (Cd, Na, O): open-circuit voltage (V_{oc}), short circuit current density (J_{sc}), fill factor (FF) and power conversion efficiency (PCE). As can be seen, with a decrease in the band gap in CZTS: Cd, CZTS: O, the open circuit voltage V_{oc} noticeably decreases from ~ 0.3 V to 0.19 V and 0.16 V, respectively. Also, a decrease in the band gap leads to a slight increase in the short-circuit current density from 27.6 mA / cm^2 to 30.41 mA/cm^2. Despite the small dose of Cd, Na, O impurities, their presence leads to a decrease in the PCE of solar cells. PCE decreases from ~ 5 % to 2.34 %.

Table 1. The Main Output Energy Parameters

	Voc, V	Jsc, mA/cm^2	FF, %	PCE, %
CZTS	0.297	27.595	60.58	4.97
CZTS:Cd	0.187	30.282	46.07	2.61
CZTS:Na	0.277	25.674	56.37	3.3
CZTS:O	0.157	30.409	49.22	2.34

One of the main characteristics of solar cells is the JV characteristic (Fig. 5). The JV characteristic reflects the internal dynamics of a solar cell and shows the parameters that determine its output power. As can be seen, a solar cell based on an absorber contaminated with Cd, Na, O has relatively worse JV characteristics and is significantly inferior in output power from a solar cell based on a pure absorber.

The quantum yield of a solar cell based on a pure and impurity absorber is shown in Fig. 6. The quantum yield of solar cells with CZTS: Cd and CZTS: O is noticeably inferior to that of a pure absorber in the high-energy region (~ 2.8–4 eV), and in the case of CZTS: Na, on the contrary, in the low-energy region (~ 1.5–2.5 eV). We believe that this is due to a change in the band gap towards a decrease in CZTS: Cd (E_g ~ 0.9 eV) and CZTS: O (E_g ~ 0.79 eV) and an increase in the case of CZTS: Na (E_g~1.2 eV), as well as a change in their optical characteristics.

In the end, it should be noted that the important role in the functioning of various devices, including solar cells, depends on the state of their surface, defects on the surface and in the near-surface layer, surface porosity, stability of adsorbed molecules, etc. [32]–[45]. Some of these issues are in progress and will be reported in subsequent articles.

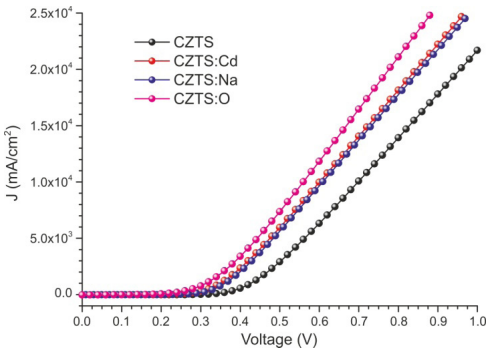

Fig. 5. JV characteristics of a solar cell based on CZTS.

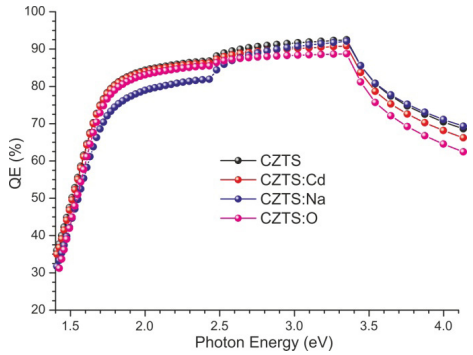

Fig. 6. CZTS based solar cell quantum yield.

4. CONCLUSIONS

Thus, in this paper, within the framework of the DFT-GGA, the optical properties of the CZTS multicomponent semiconductor absorber with a 3 % impurity of Cd, Na, O were determined, as well as their effect on the performance of CZTS solar cells was considered. It was shown that the introduction of these impurities would lead to a decrease in the intensity of the absorption spectrum at 2.06 eV and 2.55 eV. It was

revealed that impurities of Cd and O atoms would lead to a decrease in E_g CZTS to 0.9 eV and 0.79 eV, respectively, while impurities of Na atoms increased E_g to 1.2 eV. It was found that with a decrease in the band gap in CZTS: Cd, CZTS:O, the open circuit voltage V_{oc} noticeably decreased from ~ 0.3 V to 0.19 V and 0.16 V, and the indicated impurities led to a decrease in the PCE of solar cells from ~ 5 % to 2.34 %. It was shown that solar cells with impurity absorbers had poorer JV characteristics, and their quantum yield was noticeably inferior to those of a pure absorber both in the high-energy region (CZTS: Cd, CZTS: O) and in the low-energy region (CZTS: Na). The results obtained can be useful in the development of environmentally-friendly solar cells based on CZTS for future technologies.

ACKNOWLEDGEMENTS

The research has been supported by grant of the Ministry of Education and Science of the Republic of Kazakhstan AP09562784. The authors (D. Sergeyev) acknowledges the provision of SCAPS-1D software by Prof. Marc Burgelman. The research of A.I. Popov has been supported by the Institute of Solid State Physics (ISSP), University of Latvia (UL). ISSP UL as the Centre of Excellence is supported through the Framework Program for European Universities Union Horizon 2020, H2020-WIDESPREAD-01–2016–2017-TeamingPhase2 under Grant Agreement No. 739508, CAMART2 project.

REFERENCES

1. Khan, M.R., Patel, M.T., Asadpour, R., Imran, H., Butt, N.Z., & Alam, M.A. (2021). A Review of Next Generation Bifacial Solar Farms: Predictive Modeling of Energy Yield, Economics, and Reliability. *Journal of Physics D-Applied Physics*, 54 (32), 323001. DOI: 10.1088/1361-6463/abfce5
2. Veremiichuk, Y., Yarmoliuk, O., Pustovyi, A., Mahnitko, A., Zicmane, I., & Lomane, T. (2020). Features of Electricity Distribution Using Energy Storage in Solar Photovoltaic Structure. *Latvian Journal of Physics and Technical Sciences*, *5*, 18–29. DOI: 10.2478/lpts-2020-0024
3. Tao, L., Qiu, J., Sun, B., Wang, X., Ran, X., Song, L., …, & Chen, Y. (2021). Stability of Mixed-Halide Wide Bandgap Perovskite Solar Cells: Strategies and Progress. *Journal of Energy Chemistry*, *61*, 395–415. DOI: 10.1016/j.jechem.2021.03.0382095-4956
4. Bezrukovs, D., Bezrukovs, V., Bezrukovs, Vl., Konuhova, M., & Aniskevich, S. (2020). The Comparison of the Efficiency of Small Wind Turbine Generators with Horizontal and Vertical Axis under Low Wind Conditions. *Latvian Journal of Physics and Technical Sciences*, *5*, 61–72. DOI: 10.2478/lpts-2020-0028
5. Groza, E., Balodis, M., Gulbis, K., & Dirba, J. (2021). Benefits of Energy Storage Systems for Small-Scale Wind Farm Development in Latvia. *Latvian Journal of Physics and Technical Sciences*, *2*, 11–18. DOI: 10.2478/lpts-2021-0008
6. Trota, A., Ferreira, P., Gomes, L., Cabral, J., & Kallberg, P. (2019). Power Production Estimates from Geothermal Resources by Means of Small-Size Compact Climeon Heat Power Converters: Case Studies from Portugal (Sete Cidades, Azores and Longroiva Spa, Mainland). *Energies*, *12* (14), 2838. DOI: 10.3390/en12142838

7. Ciceron, J., Badel, A., & Tixador, P. (2017). Superconducting Magnetic Energy Storage and Superconducting Self-Supplied Electromagnetic Launcher. *European Physical Journal – Applied Physics*, *80* (2), 20901. DOI: 10.1051/epjap/2017160452
8. Zhang, Y., Jia, X., Liu, S., Zhang, B., Lin, K., Zhang, J., & Conibeer, G. (2021). A Review on Thermalization Mechanisms and Prospect Absorber Materials for the Hot Carrier Solar Cells. *Solar Energy Materials and Solar Cells*, *225*, 111073. DOI: 10.1016/j.solmat.2021.111073
9. Bello, M., & Shanmugan, S. (2020). Achievements in Mid and High-Temperature Selective Absorber Coatings by Physical Vapor Deposition (PVD) for Solar Thermal Application. *Journal of Alloys and Compounds*, *839*, 155510. DOI: 10.1016/j.jallcom.2020.155510
10. Kaulachs, I., Ivanova, A., Holsts, A., Roze, M., Flerov, A., Tokmakov, A., …, & Rutkis, M. (2021). Perovskite $CH_3NH_3PbI_{3-x}Cl_x$ Solar Cells. Experimental Study of Initial Degradation Kinetics and Fill Factor Spectral Dependence. *Latvian Journal of Physics and Technical Sciences*, *1*, 53–69. DOI: 10.2478/lpts-2021-0006
11. Mandal, P., Debbarma, J., & Saha, M. (2021). A Review on the Emergence of Graphene in Photovoltaics Industry. *Biointerface Research in Applied Chemistry*, *11* (6), 15009–15036. DOI: 10.33263/BRIAC116.1500915036
12. Sergeyev, D.M., & Duisenova, A.G. (2021). Electron Transport in Model Quasi-Two-Dimensional van der Waals Nanodevices. *Technical Physics Letters*, *47* (4), 375–378. DOI: 10.1134/S1063785021040295
13. Meng, Zh., Stolz, R.M., Mendecki, L., & Mirica, K.A. (2019). Electrically-Transduced Chemical Sensors Based on Two-Dimensional Nanomaterials. *Chem. Rev*, *119*, 478–598. DOI: 10.1021/acs.chemrev.8b00311
14. Koch, R.J., Konstantinova, T., Abeykoon, M., Wang, A., Petrovic, C., Zhu, Y., …, & Billinge, L. (2019). Room Temperature Local Nematicity in FeSe Superconductor. *Phys. Rev. B, 100*, 020501. DOI:10.1103/PhysRevB.100.020501
15. Sergeyev, D.M. (2013). Plasma Frequency in Josephson Junctions with a Non-Sinusoidal Current-Phase Relation. *Solid State Phenomena*, *200*, 272–275. DOI: 10.4028/www.scientific.net/SSP.200.272
16. Sergeyev, D.M. (2012). About Tunneling of Pairs of the Cooper Pairs through the Josephson Junctions in Exotic Superconductors. *Russian Physics Journal*, *55* (1), 84–91. DOI: 10.1007/s11182-012-9779-4
17. Balakhayeva, R., Akilbekov, A., Baimukhanov, Z., Usseinov, A., Giniyatova, S., Zdorovets, M., …, & Dauletbekova, A. (2021). CdTe Nanocrystal Synthesis in SiO2/Si Ion-Track Template: The Study of Electronic and Structural Properties. *Physica Status Solidi A*, *218* (1), 2000231. DOI: 10.1002/pssa.202000231
18. Sergeyev, D.M. (2018). Computer Simulation of Electrical Characteristics of a Graphene Cluster with Stone-Wales Defects. *J. Nano-Electron. Phys., 10* (3), 03018. DOI: 10.21272/jnep.10(3).03018
19. Chuan, M.W., Lau, J.Y., Wong, K.L., Hamzah, A., Alias, N.E., Lim, C.S., & Tan, M.L.P. (2021). Low-Dimensional Modelling of n-Type Doped Silicene and its Carrier Transport Properties for Nanoelectronic Applications. *Advances in Nano Reseach*, *10* (5), 415–422. DOI: 10.12989/anr.2021.10.5.415
20. Sergeyev, D. (2021). One-Dimensional Schottky Nanodiode Based on Telescoping Polyprismanes. *Advances in Nano Reseach*, *10* (4), 339–347. DOI: 10.12989/anr.2021.10.4.339
21. Zeng, X., Lontchi, J., Zhukova, M., Fourdrinier, L., Qadir, I., Ren, Y., …, & Flandre, D. (2021). High-Responsivity Broadband Photodetection of an Ultra-Thin In_2S_3/CIGS Heterojunction on Steel. *Optics Letters*, *46* (10), 2288–2291. DOI: 10.1364/OL.423999
22. Witte, W., Hempel, W., Paetel, S., Menner, R., & Hariskos, D. (2021). Effects of Sputtered In_xS_y Buffer on CIGS with RbF Post-Deposition Treatment. *ECS Journal of Solid State Science and Technology*, *10* (5), 055006. DOI: 10.1149/2162-8777/abfc21

23. Yang, H., Jiang, G., Wang, W., & Mei, X. (2021). Femtosecond Laser Fabrication of Micro and Nano-Structures on CIGS/ITO Bilayer Films for Thin-Film Solar Cells. *Materials*, *14* (9), 2413. DOI: 10.3390/ma14092413
24. Novikov, G.F., & Gapanovich, M.V. (2017). Third Generation Cu-In-Ga-(S,-Se) Based Solar Inverters. *Phys. Usp*., *60*, 161–178. DOI: 10.3367/UFNe.2016.06.037827
25. Milichko, V.A., Shalin, A.S., Mukhin, I.S., Kovrov, A.E., Krasilin, A.A., Vinogradov, A.V., …, & Simovskii, C.R. (2016). Solar Photovoltaics: Current State and Trends. *Phys. Usp*., *59*, 727–772.DOI: 10.3367/UFNe.2016.02.037703
26. Smidstrup, S., Stradi, D., Wellendorff, J., Khomyakov, P.A., Vej-Hansen, U.G., Lee, M-E., …, & Stokbro, K. (2017). First-Principles Green's-Function Method for Surface Calculations: A Pseudopotential Localized Basis Set Approach, *Phys. Rev. B*, *96*, 195309. DOI: 10.1103/PhysRevB.96.195309
27. *Atomistix ToolKit*. Manual Version. (2015). *QuantumWise A/S,* 1, 840.
28. Burgelman, M., Nollet, P., & Degrave, S. (2000). Modelling Polycrystalline Semiconductor Solar Cells. *Thin Solid Films*, *361–362*, 527–532. DOI: 10.1016/S0040-6090(99)00825-1
29. Decock, K., Zabierowski, P., & Burgelman, M. (2012). Modeling Metastabilities in Chalcopyrite-Based Thin Film Solar Cells. *Journal of Applied Physics*, *111*, 043703. DOI: 10.1063/1.3686651
30. Burgelman, M., Decock, K., Khelifi, S., & Abass, A. (2013). Advanced Electrical Simulation of Thin Film Solar Cells. *Thin Solid Films*, *535*, 296–301. DOI: 10.1016/j.tsf.2012.10.032
31. Decock, K., Khelifi, S., & Burgelman, M. (2011). Modelling Multivalent Defects in Thin Film Solar Cells. *Thin Solid Films*, *519*, 7481–7484. DOI: 10.1016/j.tsf.2010.12.039
32. Sychikova, Y.A., Kidalov, V.V., & Sukach, G.A. (2013). Dependence of the Threshold Voltage in Indium-Phosphide Pore Formation on the Electrolyte Composition. *J. Synch. Investig., 7,* 626–630. DOI: 10.1134/S1027451013030130
33. Suchikova, J. A. (2015). Synthesis of Indium Nitride Epitaxial Layers on a Substrate of Porous Indium Phosphide. *Journal of Nano- and Electronic Physics*, *7* (3), 3017–1.
34. Eglitis, R., Purans, J., Popov, A. I., & Jia, R. (2019). Systematic Trends in $YAlO_3$, $SrTiO_3$, $BaTiO_3$, $BaZrO_3$ (001) and (111) Surface *ab initio* Calculations. *International Journal of Modern Physics B*, *33* (32), 1950390. DOI: 10.1142/S0217979219503909
35. Eglitis, R., Popov, A. I., Purans, J., & Jia, R. (2020). First Principles Hybrid Hartree-Fock-DFT Calculations of Bulk and (001) Surface F Centers in Oxide Perovskites and Alkaline-Earth Fluorides. *Low Temperature Physics*, *46* (12), 1206–1212. DOI: 10.1063/10.0002475
36. Eglitis, R. I., Purans, J., Gabrusenoks, J., Popov, A. I., & Jia, R. (2020). Comparative *ab initio* Calculations of ReO_3, $SrZrO_3$, $BaZrO_3$, $PbZrO_3$ and $CaZrO_3$ (001) Surfaces. *Crystals*, *10* (9), 745. DOI: 10.3390/cryst10090745
37. Rusevich, L. L., Kotomin, E. A., Zvejnieks, G., & Popov, A. I. (2020). *Ab initio* Calculations of Structural, Electronic and Vibrational Properties of $BaTiO_3$ and $SrTiO_3$ Perovskite Crystals with Oxygen Vacancies. *Low Temperature Physics*, *46* (12), 1185–1195. DOI: 10.1063/10.0002472
38. Krainyukova, N. V., Hamalii, V. O., Peschanskii, A. V., Popov, A. I., & Kotomin, E. A. (2020). Low Temperature Structural Transformations on the (001) Surface of SrTiO3 Single Crystals. *Low Temperature Physics*, *46* (7), 740–750. DOI: 10.1063/10.0001372
39. Krainyukova, N. V., Kuchta, B., Firlej, L., & Pfeifer, P. (2020). Absorption of Atomic and Molecular Species in Carbon Cellular Structures. *Low Temperature Physics*, *46* (3), 219–231. DOI: 10.1063/10.0000705
40. Suchikova, Y., Vambol, S., Vambol, V., & Mozaffari, N. (2019). Justification of the Most Rational Method for the Nanostructures Synthesis on the Semiconductors Surface. *Journal of Achievements in Materials and Manufacturing Engineering*, *92* (1–2), 19–28.

41. Ananyev, M. V., Porotnikova, N. M., & Kurumchin, E. K. (2019). Influence of Strontium Content on the Oxygen Surface Exchange Kinetics and Oxygen Diffusion in $La_{1-x}Sr_xCoO_{3-\delta}$ Oxides. *Solid State Ionics*, *341*, 115052. DOI: 10.1016/j.ssi.2019.115052

42. Osinkin, D.A., Khodimchuk, A.V., Porotnikova, N.M., Bogdanovich, N.M., Fetisov, A.V., & Ananyev, M.V. (2020). Rate-Determining Steps of Oxygen Surface Exchange Kinetics on $Sr_2Fe_{1.5}Mo_{0.5}O_{6-\delta}$. *Energies*, *13*, 250. DOI: 10.3390/en13010250

43. Porotnikova, N. M., Vlasov, M. I., Zhukov, Y., Kirschfeld, C., Khodimchuk, A. V., Kurumchin, E. K., ..., & Ananyev, M. V. (2021). Correlation between Structure, Surface Defect Chemistry and $^{18}O/^{16}O$ Exchange for $La_2Mo_2O_9$ and $La_2(MoO_4)_3$. *Physical Chemistry Chemical Physics*, *23* (22), 12739–12748. DOI: 10.1039/D1CP00401H

44. Hamalii, V. O., Peschanskii, A. V., Popov, A. I., & Krainyukova, N. V. (2020). Intrinsic Nanostructures on the (001) Surface of Strontium Titanate at Low Temperatures. *Low Temperature Physics*, *46* (12), 1170–1177. DOI: 10.1063/10.0002470

45. Ostanina, T. N., Rudoi, V. M., Nikitin, V. S., Darintseva, A. B., Zalesova, O. L., & Porotnikova, N. M. (2016). Determination of the Surface of Dendritic Electrolytic Zinc Powders and Evaluation of its Fractal Dimension. *Russian Journal of Non-Ferrous Metals*, *57* (1), 47–51. DOI: 10.3103/S1067821216010120

sciendo

LATVIAN JOURNAL OF PHYSICS
AND TECHNICAL SCIENCES
2021, N 6

DOI: 10.2478/lpts-2021-0043

WO_3 AS ADDITIVE FOR EFFICIENT PHOTOCATALYST BINARY SYSTEM TiO_2/WO_3

A. Knoks*, J. Kleperis, G. Bajars, L. Grinberga, O. Bogdanova

Institute of Solid State Physics, University of Latvia,
8 Kengaraga Str., Riga, LV-1063, LATVIA
*e-pasts: knoks@cfi.lu.lv

Two different methods of synthesis of TiO_2/WO_3 heterostructures were carried out with the aim to increase photocatalytic activity. In this study, anodic TiO_2 nanotube films were synthesized by electrochemical anodization of titanium foil. WO_3 particles were applied to anodic Ti/TiO_2 samples in two different ways – by electrophoretic deposition (EPD) and insertion during the anodization process. Structural and photocatalytic properties were compared between pristine TiO_2 and TiO_2 with incorporated WO_3 particles. Raman mapping was used to characterise the uniformity of EPD WO_3 coating and to determine the structural composition. The study showed that deposition of WO_3 onto TiO_2 nanotube layer lowered the band gap of the binary system compared to pristine TiO_2 and WO_3 influence on photo-electrochemical properties of titania. The addition of WO_3 increased charge carrier dynamics but did not increase the measured photocurrent response. As the WO_3 undergoes a phase transition from monoclinic to orthorhombic at approximately 320 °C proper sequence WO_3 deposition could be beneficial. It was observed that secondary heat treatment of WO_3 lowers the photocurrent.

Keywords: *Anodization, electrophoretic deposition, TiO_2 nanotubes, thin films, TiO_2/WO_3, WO_3.*

1. INTRODUCTION

In search of new sustainable energy sources, photocatalysis is a prominent area of research. However, synthesis of materials for an efficient photocatalytic cell still is a great challenge. Titanium dioxide (TiO_2, titania) is extensively studied as a possible candidate owing to abundance, stability, and synthesis options. Nanostructured titania can be synthesized in a great variety of methods, i.e., sol-gel [1], physical vapour deposition PVD [2], magnetron sputtering [3], electrochemical anodization [4]. The

increased active surface area is desirable; therefore, electrochemical anodization is preferred as anodic TiO_2 forms a self-organized nanotube layer with a high surface area and geometry, enables high charge transfer and electron percolation [5]–[7], and the method is energy and cost-effective with a potential for scale-up [8].

Photocatalytic activity of TiO_2 was discovered only in 1972 by Fujishima and Honda [9], although TiO_2 had been used for decades in various everyday applications, such as gas sensing, colouring pigment, additive for food, toothpaste [10]–[12]. The process of photocatalytic water splitting happens thanks to absorbed photons with energy at least as a band gap of TiO_2, creating electron-hole pair (e-h), which must be separated before recombination [13]. Electrons are collected by current conductor and transferred to the cathode, but holes migrate to the surface and drive a catalytic reaction (splitting H_2O, organic/inorganic pollutants, gas-phase pollutants, etc.) reducing or oxidating molecules [14].

The potential of generated charge carriers must be sufficient to reduce target molecule, TiO_2 conduction and valence bands are at a sufficient level. However, titania has a wide band gap reaching in the UV region ($\lambda \leq 380$ nm), thus limiting the use of sunlight as the light source for activation. Combination of TiO_2 with other photocatalytic materials, which are sensitive in the visible light region, could solve this problem, as it was shown in [15]–[18]. The tungsten trioxide (WO_3) – a comparatively less studied photocatalytically active semiconducting oxide (n-type) – is capable of being activated by visible light in the blue region with $\lambda \leq 450$ nm [19].

It has been shown that WO_3 incorporation in TiO_2 is a viable method. A single-step anodization process for WO_3-doped TiO_2 nanotubes in an aqueous electrolyte containing the tungsten precursor $Na_2WO_4 \cdot 2H_2O$ and fluoride ions is characterised by homogenous doping of WO_3 into the TiO_2 nanotube structures [20]. The doping concentration depends on the concentration of the tungsten precursor in the electrolyte, demonstrating that the reported anodizing process is the most efficient approach for metal oxide doping in TiO_2 [21]. For example, the incorporation of WO_3 species onto TiO_2 nanotubes also improved the mercury removal performance due to improved charge separation and decreased charge carrier recombination due to the charge transfer from the conduction band of TiO_2 to the conduction band of WO_3 [22].

In our study, the combination of anodically grown TiO_2 nanotubes with WO_3 is achieved through electrophoretic deposition (EPD) and simultaneous synthesis of TiO_2/WO_3. Anodization of TiO_2 and EPD of WO_3 are time and cost-effective methods, providing high photochemical stability and usage of non-toxic materials. The potential of WO_3 deposition and secondary treatment must be understood for successful TiO_2/WO_3 system description [15], [23]. Single-step Ti anodization with simultaneous incorporating of WO_3 microcrystalline powder was tested by pouring WO_3 into an electrolyte and mixing with a magnetic stirrer during the anodization process.

2. EXPERIMENTAL

TiO_2 nanotubes were synthesized by electrochemically anodizing titanium (Ti) foil (0.5 mm, Sigma Aldrich) in water-based electrolyte. Ti foil was cleaned and polished

(abrasive material Cr_2O_3 (Sigma Aldrich), average particle size 400 nm), then ultrasonicated for 10 min in acetone (99 % Sigma-Aldrich) and dried in ambient atmosphere. Anodization was performed in two steps: 1) 5 V applied for 10 minutes, 2) 20 V applied for 90 minutes with electrode separation of 2 cm. It is known that anodizing in water based electrolytes requires F^- ions for TiO_2 dissolution as reported by Regonini [24] and Grimes [5]; NaF (Sigma Aldrich) was used as F^- ion source. pH was adjusted with 1M NaOH (Sigma Aldrich) solution until pH level of 4. Anodized samples were rinsed in deionized water and dried in ambient atmosphere. To obtain crystalline TiO_2 samples were heat treated in a furnace at 500 ºC for 120 minutes, heating speed 5 ºC/min and natural cooling. WO_3 (powder from Sigma Aldrich) was deposited on Ti/TiO_2 via EPD from isopropanol/HCl electrolyte (both from Sigma Aldrich) in volume ratio 150:1 with WO_3 particles mixed by vigorous stirring and ultrasonication until homogeneous distribution was achieved. EPD process and experimental setup was used similar to the one described by Liepina et al. [15]. Working and auxiliary electrodes were respectively Ti/TiO_2 and platinum foil (0.2 mm, Sigma Aldrich). Deposition was performed for various time intervals under constant potential. In this study, three sample series were produced indicated with the following identifiers: AT – pristine anodized TiO_2, EW – deposited WO_3 on anodized TiO_2 and AW – anodized TiO_2 with WO_3 particles present in the electrolyte. Production of AW follows AT procedure, where electrolyte contains dispersed WO_3 particles.

Morphological properties were determined by scanning electron microscope (Phenom Pro). Structural properties were determined by Raman spectroscopy (RENISHAW inVia Raman Microscope) and X-Ray diffraction (X-ray Diffractometer X'Pert Pro MPD, Cu anode, λ = 0.154 nm). Optical band gap was calculated from reflectance spectra, acquired in 240 to 780 nm range, using integrating sphere in spectrophotometer (Shimadzu SolidSpec-3700). Photoactivity was determined using three-electrode cell, where AT, EW and AW samples were used as working electrode; Pt and calomel (SCE) were used respectively as auxiliary and reference electrodes in 1M NaOH electrolyte. Photoactivity measurement data were collected by potentiostat VoltaLab 40 (PGZ301 Radiometer analytical) while using the visible region of 150 W xenon lamp as a light source. The sample EW synthesis process is shown in Fig. 1.

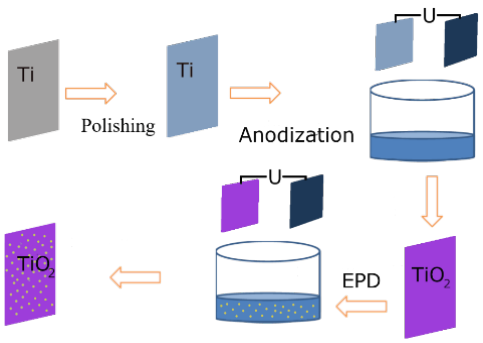

Fig. 1. Sample synthesis procedure: Ti is polished, then anodized in electrolyte without or with WO_3 (in case of single-step AW sample the tungsten oxide particles were dispersed in anodization electrolyte). In a two-step process (below), anodic TiO_2 is heat treated, then WO_3 deposited using EPD.

3. RESULTS AND DISCUSSION

Morphology of the obtained samples was investigated before and after EPD. As it can be seen in SEM images (Fig. 2a), TiO_2 was synthesized in nanosized tubular forms. EPD of WO_3 covers TiO_2 partially as seen in Fig. 2b.

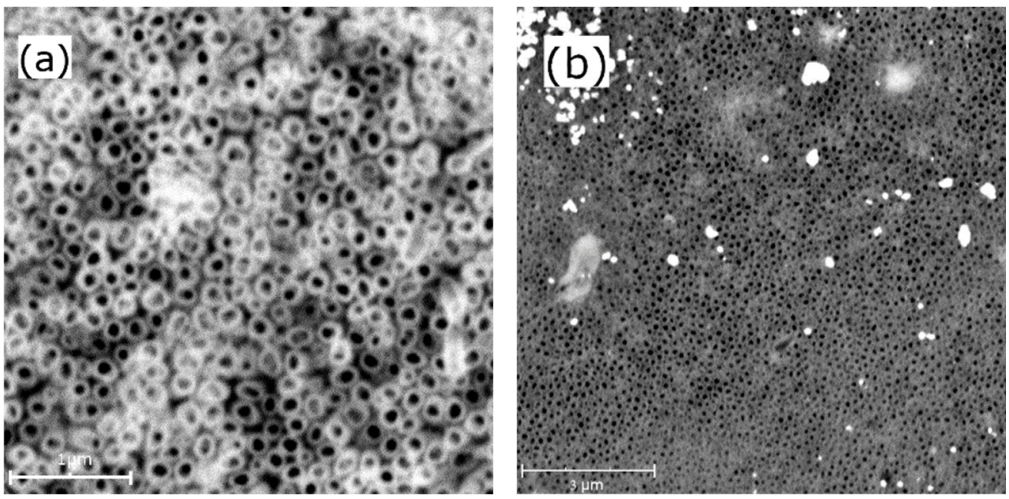

Fig. 2. Morphology investigation with SEM: (a) tubular structures of TiO_2 in an anodized sample, (b) TiO_2 nanotube layer decorated with WO_3 microparticles.

As measured from SEM photo (Fig. 2b), the average dimensions of WO_3 particles are 150–250 nm. It is also seen that microparticles result from the agglomeration of WO_3 nanocrystals, thus indicating the importance of sonication for even distribution as well as appropriate EPD parameters. It is known that amount threshold of WO_3 deposition exists [25], where overdeposition shows lower photo-activity; thus, the only appropriate correct amount can enhance photoelectrochemical properties [15], [26].

Sample crystallinity and the presence of WO_3 and TiO_2 were determined through XRD. As it can be seen in Fig. 3, the WO_3 is present in sample EW, but the AW sample does not show monoclinic WO_3 structure indicating the undergoing phase transition during sample preparation. The change is clearly seen in the typical 2θ mode intensity of peaks at 22º, 23º, and 24º. The size of WO_3 crystallites was evaluated from Scherrer equation (Patterson et al. [27]), using parameters of the peak 2θ=23º – 40±5 nm, whereas TiO_2 crystallite size – 17±3 nm was calculated for 2θ=25º. It is well known that crystallite size from XRD scattering is a qualitative indicator. The high-intensity Ti peak in the diffraction spectra comes from the Ti substrate as the radiation penetration is much deeper compared to the overall thickness of the samples. On the other hand, AT samples showed standard TiO_2 anatase phase, i.e., (101) peak at 2θ = 25º was present.

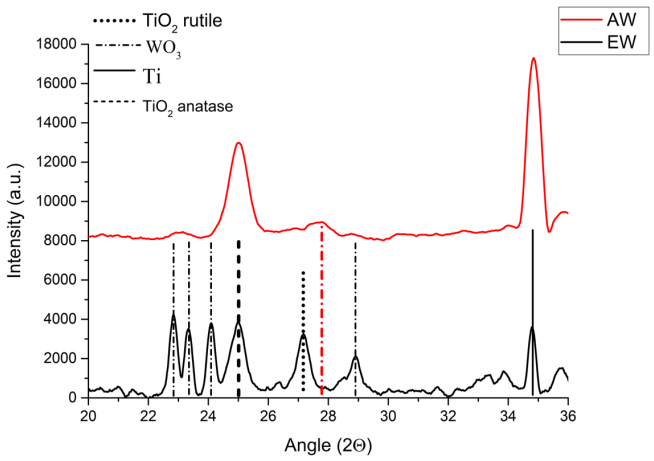

Fig. 3. XRD diffractogram of EW (in black) and AW (in red), strong Ti peaks from the substrate, distinctive WO_3 peaks below 25°, TiO_2 rutile peak at 27°. XRD diffractogram confirms that EW sample contains WO_3 as seen by specific monoclinic peak trio and not present in AW with the absence of those.

Raman investigation shows characteristic WO_3 band at 272 cm^{-1} band (Fig. 4a and 4c), similar to 270 cm^{-1} [28] and 262 cm^{-1} [29]. Particle size directly affects Raman band position, nanosized particles show a shift in Raman band positions [29]. It confirms that our WO_3 has smaller particles, large grain surfaces, and developed grain boundaries, higher concentration of structural defects.

For more comprehensive surface structural composition, the Raman mapping was performed. As seen in Fig. 4 b, c, and d, where phase distribution provides insight not only into the overall phase composition of samples, but also into uniformity of the sample structure. Sample before EPD can be seen in Fig. 4b, it shows TiO_2 composition of two phases, rutile majority with anatase spots. After EPD, WO_3 particles were found on TiO_2 surface as shown in Fig. 4c. It is possible to imagine the particle distribution on the surface using colour differentiation by phase. By assigning a colour to a single-phase the surface phase map can be created as seen in Fig. 4d, where red and green represent TiO_2 and WO_3, respectively. It shows a single particle on the TiO_2 surface.

Optical band gap (E_{gap}) was determined from reflectance spectra using Kubelka-Munk equation to find absorption edge by plotting , as seen in Fig. 5, where *n* is determined by the electron transition nature – indirect allowed transition in case of TiO_2. The same methodology can be applied for WO_3 – the monoclinic phase has direct allowed transitions and orthorhombic – indirect allowed transitions [30]. Introduction of WO_3 clearly lowers the optical band gap as seen in sample EW (Fig. 5a). Pristine anatase TiO_2 optical band gap is close to the theoretical value of 3.1 eV; similarly, the AW has 3.1 eV optical band gap. After EPD of WO_3, the optical band gap lowered to 2.86 eV.

As the directly incorporated WO_3 undergoes heat treatment, anodized titania is amorphous after synthesis, the influence of annealing should be estimated. Samples from EW series were compared as-prepared and with secondary heat treatment. Figure 5b shows that a small increase in the optical band gap is present. Thus, photoelectrochemical properties could also be changed. Diaz-Reyes et al. [31] also reported an increase in the band gap of WO_3 after the heat treatment, where they suggested higher crystallinity and oxygen vacancies as the reason for change.

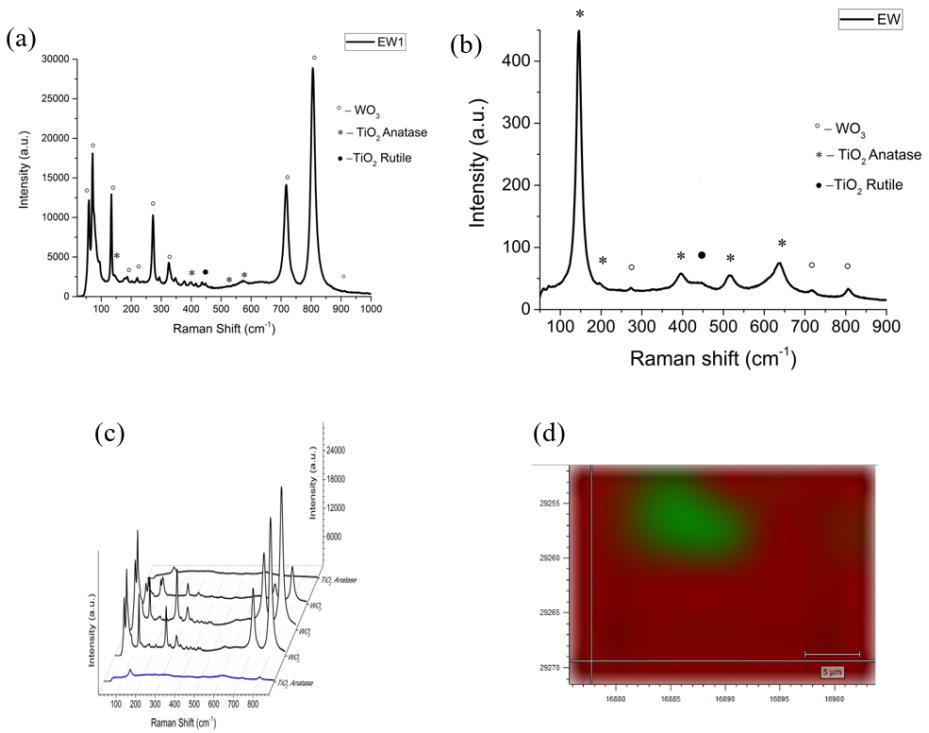

Fig. 4. (a) Raman spectra of WO_3 for EW sample; (b) TiO_2 Raman spectra for EW in another position – clear TiO_2 anatase bands and Rutile bands are seen; (c) Raman mapping of EW sample, WO_3 bands with high intensity and low intensity anatase TiO_2; (d) EW sample in 2D composition/structural distribution of both materials – TiO_2 (red), WO_3 (green).

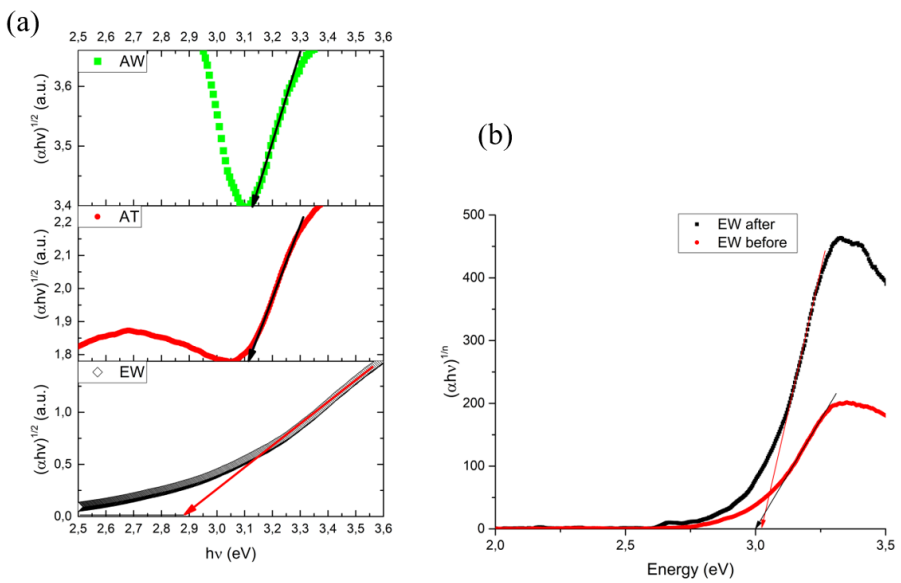

Fig. 5. (a) E_{gap} comparison between various samples; (b) optical band gap comparison for WO_3/TiO_2 deposited with EPD before and after heat treatment.

Photoactivity was determined by measuring photocurrent response (PCR) – voltage transient characteristics – see Fig. 6c, and open circuit potential (OCP) – see Fig. 6b and 6d. In addition, the Mott-Schottky method was used to determine charge carrier density. Comparing PCR values for samples before and after EPD there can be an increase in PCR and OCP values as provided in the literature showing that WO_3 deposition on TiO_2 can have a positive effect on photoactivity.

Upon deposition of WO_3 a certain limit has to be maintained, as overdeposition of WO_3 has a negative impact on photoactivity as seen in Fig. 6a. A test sample in EW series was overdeposited and ultrasonically cleaned to decrease WO_3 amount on the surface; OCP value rose again as seen in Fig. 6a red plot. In this study, for EPD the electric field was kept at 5–6 V/cm considering lower necessary deposition time. With higher deposition times, the film thickness easily saturates within minutes with deposited layer over 60 μm, lowering a photo-electrochemical activity as shown in Fig. 6a. Such observation supports the necessity to find equilibrium and even distribution of WO_3 particles on TiO_2 for an increase in activity. Similar findings were reported by Khoo et al. [25]. Comparing annealing influence on the PCR and OCP, PCR and OCP decreased by 70 % and 75 %, respectively (see Fig. 6b). The change could be attributed to change in crystallinity and phase transition from monoclinic to triclinic as seen in structural analysis. Thus, it is not surprising that sample AW provides similar results, showing 55 % and 36 % decrease in OCP and PCR, respectively, and EW shows 65 % and 48 % decrease, respectively, as seen in Fig. 6c and d as well as in Table 1. Though, it is noteworthy that AW shows higher charge carrier dynamics indicating more rapid higher charge carrier separation compared to AT dynamics, where reaching plato takes more time. Dynamics can be seen in Fig. 6c – PCR and Fig. 6d – OCP.

Amount of WO_3 on/in TiO_2 is critical for a higher photocatalytic activity, which is confirmed by existence of WO_3 amount threshold for the increased photo-physical activity [10]. Existence of a threshold is determined by generated charge carrier interfacial transfer, thereof it stops over the threshold when most of the light is absorbed by WO_3 and as material with lower photocurrent values the result shows overall lower photocurrent. It can be assumed that generated e-h pairs go through charge interfacial transfer, hole from valence band (V_B) of WO_3 to V_B of TiO_2 and e^- from TiO_2 conduction band (C_B) to WO_3 C_B. Estimation of charge carrier density shows that addition of WO_3 in both series (EW and AW) provides with two orders of magnitude higher charge carrier density compared to AT samples. For AW, the great change is seen in PCR dynamics, but an absolute value did not increase.

Table 1. Summary of Results (OCP and PCR – photoactivity, E_{gap} – optical band, E_{Fb} – flat band potential and N_D – charge carrier density)

Sample	OCP, mV	PCR, μA/cm^2	E_{gap}, eV	E_{Fb}, mV	N_D (cm^{-3})
AT	-222.6±4.7	4.01±0.79	3.11±0.04	-1919.4±0.2	$4.7 \cdot 10^{17}$
EW	-80.5	2.07	2.86	-668.8	$1.6 \cdot 10^{21}$
AW	-99.3	2.63	3.13	-799.3	$6.1 \cdot 10^{21}$

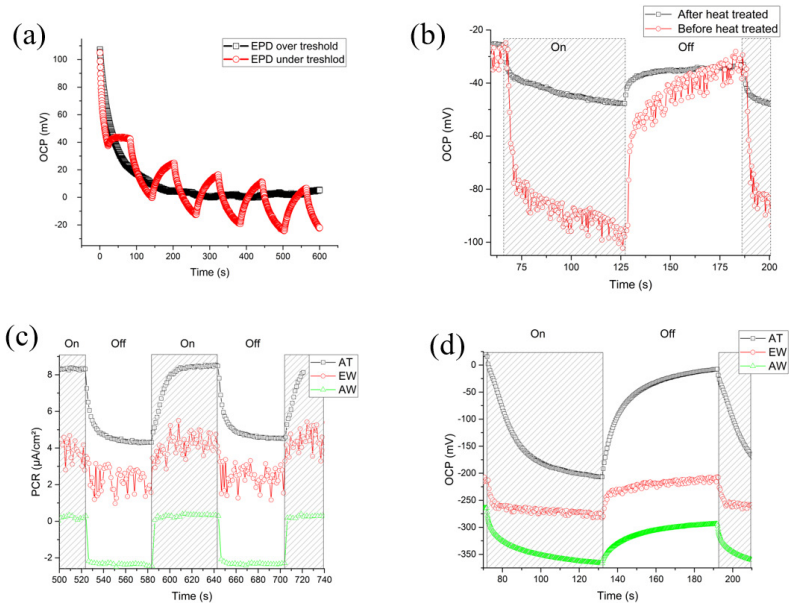

Fig. 6. Sample photoactivity dependence and comparison. (a) OCP value comparison of WO_3 deposition amount. Overdeposition decreases OCP. (b) OCP value comparison for WO_3 before and after heat treatment. (c) PCR comparison of samples, AW has the highest charge separation, EW shows low PCR values and a high recombination rate. (d) OCP comparison for samples, AT shows the highest OCP.

4. CONCLUSIONS

In this study, different methods of synthesis and investigation of $Ti/TiO_2/WO_3$ system were carried out. Firstly, anodic titania was synthesized. Secondly, electrophoretic deposition of WO_3 particles on the surface of an anodically grown TiO_2 nanotube layer done. Thirdly, a single-step Ti anodization with simultaneous incorporating of WO_3 microcrystalline powder was performed by the addition of WO_3 in the anodization process. Morphological and structural investigation of samples showed that WO_3 formed separated "islands" on TiO_2 nanotube film in EPD and incorporated WO_3 in TiO_2 nanotubes in the single-step method. Characteristic WO_3 band shifts in Raman spectroscopy were observed after annealing, indicating the change in crystallinity of WO_3, the same was seen in XRD diffractograms. The presence of Raman bands, as well as XRD provided clear evidence of synthesis of $Ti/TiO_2/WO_3$ system. In the study, the addition of WO_3 introduced lower OCP, PCR values even though the optical band gap was lowered, and charge carrier density increased.

As anodic titania required annealing after synthesis, monoclinic WO_3 particle introduction did not show promise for increased photoactivity in the visible range due to a decrease in photoactivity after heating. Similarly, overdeposition of WO_3 in the EPD method on TiO_2 lowered the photo-response of samples. However, it does not exclude the possibility of a specific ratio and/or introduction of WO_3/TiO_2 for an increase in photo-response. The introduction of tungsten atoms directly into

TiO_2 structures could be beneficial through organic tungsten acids or substituting anodization cathode. Lowered activity is explained with additional trapping sites on the WO_3 grain boundaries, as well as lower WO_3 photo-activity compared to pristine TiO_2, despite the increase in charge carrier density. Further research on the incorporation of W into TiO_2 will be carried out to investigate charge carrier transfer and the increased photoactivity.

ACKNOWLEDGEMENTS

The financial support provided by Scientific Research Project for Students and Young Researchers No. SJZ/2018/9 implemented at the Institute of Solid State Physics, University of Latvia is greatly acknowledged. Institute of Solid State Physics, University of Latvia as the Center of Excellence has received funding from the European Union's Horizon 2020 Framework Programme H2020-WIDESPREAD-01-2016-2017-TeamingPhase2 under grant agreement No. 739508, project CAMART².

REFERENCES

1. Ahn, Y. (2003). Variation of Structural and Optical Properties of Sol-Gel TiO2 Thin Films with Catalyst Concentration and Calcination Temperature. *Materials Letters*, *57* (30), 4660–4666.
2. Hasan, M. M., Haseeb, A. S. M. A., Saidur, R., & Masjuki, H. H. (2008). Effects of Annealing Treatment on Optical Properties of Anatase TiO 2 Thin Films. *International Journal of Mechanical, Aerospace, Industrial, Mechatronic and Manufacturing Engineering*, *2*, 410–414.
3. Daviðsdóttir, S., Shabadi, R., Galca, A. C., Andersen, I. H., Dirscherl, K., & Ambat, R. (2014). Investigation of DC Magnetron-Sputtered TiO2 Coatings: Effect of Coating Thickness, Structure, and Morphology on Photocatalytic Activity. *Applied Surface Science*, *313*, 677–686.
4. Regonini, D., & Clemens, F. J. (2015). Anodized TiO2 Nanotubes: Effect of Anodizing Time on Film Length, Morphology and Photoelectrochemical Properties. *Materials Letters*, *142*, 97–101.
5. Grimes, C. A., & Mor, G. K. (2009). *TiO_2 Nanotube Arrays*. Boston, MA: Springer US.
6. Sofiane, S., & Bilel, M. (2016). Effect of Specific Surface Area on Photoelectrochemical Properties of TiO2 Nanotubes, Nanosheets and Nanowires Coated with TiC Thin Films. *Journal of Photochemistry and Photobiology A: Chemistry*, *324*, 126–133.
7. Arifin, K., Yunus, R. M., Minggu, L. J., & Kassim, M. B. (2021). Improvement of TiO2 nanotubes for Photoelectrochemical Water Splitting: Review. *International Journal of Hydrogen Energy*, *46* (7), 4998–5024.
8. Khaw, J. S., Curioni, M., Skeldon, P., Bowen, C. R., & Cartmell, S. H. (2019). A Novel Methodology for Economical Scale-Up of TiO2 Nanotubes Fabricated on Ti and Ti Alloys. *Journal of Nanotechnology*, *2019*.
9. Fujishima, A., & Honda, K. (1972). Electrochemical Photolysis of Water at a Semiconductor Electrode. *Nature*, *238* (5358), 37–38.
10. Varghese, O. K., Gong, D., Paulose, M., Ong, K. G., & Grimes, C. A. (2003). Hydrogen Sensing Using Titania Nanotubes. *Sensors and Actuators B: Chemical*, *93* (1–3), 338–344.

11. Wu, H., & Zhang, Z. (2011). High Photoelectrochemical Water Splitting Performance on Nitrogen Doped Double-Wall TiO 2 Nanotube Array Electrodes. *International Journal of Hydrogen Energy*, *36* (21), 13481–13487.
12. Ismail, A. A., & Bahnemann, D. W. (2014). Photochemical Splitting of Water for Hydrogen Production by Photocatalysis: A Review. *Solar Energy Materials and Solar Cells*, *128*, 85–101.
13. Osterloh, F. E. (2008m) Inorganic Materials as Catalysts for Photochemical Splitting of Water. *Chemistry of Materials*, *20* (1), 35–54.
14. Qamar, M., Drmosh, Q., Ahmed, M. I., Qamaruddin, M., & Yamani, Z. H. (2015). Enhanced Photoelectrochemical and Photocatalytic Activity of WO3-Surface Modified TiO2 Thin Film. *Nanoscale Research Letters*, *10* (1), 54.
15. Liepina, I., Bajars, G., Rublans, M., Kleperis, J., Lusis, A., & Pentjuss, E. (2015). Structure and Photocatalytic Properties of TiO_2 -WO_3 Composites Prepared by Electrophoretic Deposition. *IOP Conference Series: Materials Science and Engineering*, *77* (1), 012039.
16. Rong, X., Qiu, F., Zhang, C., Fu, L., Wang, Y., & Yang, D. (2015). Preparation, Characterization and Photocatalytic Application of TiO2-Graphene Photocatalyst under Visible Light Irradiation. *Ceramics International*, *41* (2), 2502–2511.
17. Lu, X., Ma, Y., Tian, B., & Zhang, J. (2011). Preparation and Characterization of Fe–TiO_2 Films with High Visible Photoactivity by Autoclaved-Sol Method at Low Temperature. *Solid State Sciences*, *13* (3), 625–629.
18. Ola, O., & Maroto-Valer, M. M. (2015). Transition Metal Oxide Based TiO2 Nanoparticles for Visible Light Induced CO2 Photoreduction. *Applied Catalysis A: General*, *502*, 114–121.
19. Amano, F., Ishinaga, E., & Yamakata, A. (2013). Effect of Particle Size on the Photocatalytic Activity of WO3 Particles for Water Oxidation. *Journal of Physical Chemistry C*, *117* (44), 22584–22590.
20. Riboni, F., Bettini, L. G., Bahnemann, D. W., & Selli, E. (2013). WO3-TiO2 vs. TiO2 Photocatalysts: Effect of the W Precursor and Amount on the Photocatalytic Activity of Mixed Oxides. *Catalysis Today*, *209*, 28–34.
21. Yoo, H., Oh, K., Nah, Y. C., Choi, J., & Lee, K. (2018). Single-Step Anodization for the Formation of WO_3-Doped TiO_2 Nanotubes toward Enhanced Electrochromic Performance. *ChemElectroChem*, *5* (22), 3379–3382.
22. Lee, W. H., Lai, C. W., & Abd Hamid, S. B. (2015). In Situ Anodization of WO_3-Decorated TiO_2 Nanotube Arrays for Efficient Mercury Removal. *Materials*, *8* (9), 5702–5714.
23. Nazari, M., Golestani-Fard, F., Bayati, R., & Eftekhari-Yekta, B. (2015). Enhanced Photocatalytic Activity in Anodized WO3-Loaded TiO2 Nanotubes. *Superlattices and Microstructures*, *80* (4), 91–101.
24. Regonini, D., Bowen, C. R. R., Jaroenworaluck, A., & Stevens, R. (2013). A Review of Growth Mechanism, Structure and Crystallinity of Anodized TiO2 Nanotubes. *Materials Science and Engineering R: Reports*, *74* (12), 377–406.
25. Khoo, E., Lee, P. S., & Ma, J. (2010). Electrophoretic Deposition (EPD) of WO3 Nanorods for Electrochromic Application. *Journal of the European Ceramic Society*, *30* (5), 1139–1144.
26. Lai, C. W., & Sreekantan, S. (2013). Incorporation of WO3 Species into TiO2 Nanotubes via Wet Impregnation and their Water-Splitting Performance. *Electrochimica Acta*, *87*, 294–302.
27. Patterson, A. L. (1939), The Scherrer Formula for X-Ray Particle Size Determination. *Physical Review*, *56* (10), 978–982.
28. Hunge, Y. M., Mahadik, M. A., Moholkar, A. V., & Bhosale, C. H. (2017). Photoelectrocatalytic Degradation of Oxalic Acid Using WO3 and Stratified WO3/TiO2 Photocatalysts under Sunlight Illumination. *Ultrasonics Sonochemistry*, *35*, 233–242.
29. Cai, Z.-X., Li, H.-Y., Ding, J.-C., & Guo, X. (2017). Hierarchical Flowerlike WO3 Nanostructures Assembled by Porous Nanoflakes for Enhanced NO Gas Sensing. *Sensors and Actuators B: Chemical*, *246*, 225–234.

30. Kleperis, J., Zubkans, J., & Lusis, A. R. (1997). Nature of fundamental absorption edge of WO3. In E. A. Silinsh, A. Medvids, A. R. Lusis, & A. O. Ozols (Eds.), *Optical Organic and Semiconductor Inorganic Materials* (vol. 2968, pp. 186–191). International Society for Optics and Photonics.

31. Diaz-Reyes, J., Flores-Mena, J. E., Gutierrez-Arias, J. M., Morin-Castillo, M. M., Azucena-Coyotecatl, H., Galván, M., … & Mendez-López, A. (2010). Optical and structural properties of WO_3 as a function of the annealing temperature. In *Proceedings of the 3rd WSEAS international Conference on Advances in Sensors, Signals and Materials* (pp. 99–104), 3–5 November 2010, Faro, Portugal. World Scientific and Engineering Academy and Society (WSEAS).

sciendo

LATVIAN JOURNAL OF PHYSICS
AND TECHNICAL SCIENCES
2021, N 6

DOI: 10.2478/lpts-2021-0044

METHODOLOGY FOR INCREASING THE COMPETENCES OF HOUSING MANAGERS IN CLIMATE CHANGE ISSUES

I. Geipele[1]*, A. Kundzina[1], L. Jansons[1,2]

[1]Riga Technical University,
Institute of the Civil Engineering and Real Estate Economics
6 Kalnciema Str., Riga, LV-1048, LATVIA
[1,2]Institute of Physical Energetics
11 Krīvu Str., Riga, LV-1006, LATVIA
*e-mail: Ineta.Geipele@rtu.lv

In order to identify the necessary competences and develop the study course programme, within the framework of the EUKI (The European Climate Initiative; Die Europäische Klimaschutzinitiative) project "From Housing Manager to CLImate Manager", research [1] has been conducted, describing the Latvian residential fund, analysing the principles and activities of multi-apartment residential buildings, as well as identifying and describing the parties involved in shaping the housing policy. Special attention is paid to energy efficiency issues for buildings – looking at Latvia's potential for climate changes, analysing energy consumption in buildings in relation to energy efficiency requirements, as well as assessing the medium and long-term objectives of buildings in Latvia and the obstacles to achieving them.

In order to clarify more precisely the necessary competences of housing managers for the successful implementation of the residential renovation process, a survey has been carried out for stakeholders in the project. Based on an analysis of the situation and the performed survey results, a methodology has been developed to increase the competences of housing managers in relation to the renovation of residential buildings in order to mitigate climate change.

Keywords: *Climate changes, energy efficiency, housing policy, housing management.*

1. INTRODUCTION

The Latvian National Development Plan for 2021–2027 states that energy saving and sustainable use of resources are the responsibility of society in building a sustainable life environment and ensuring a circular economy. Significant energy savings can be achieved by introducing more efficient GHG reduction measures to increase the energy efficiency of buildings and improve heat resilience [2].

Management of multi-apartment residential houses (MARH), including energy efficiency issues, concerns both residents and owners of MARH and the interests of individual residential areas, as well as the state interests in general.

In 2019, Latvia took the first place in Europe by number of residents living in apartments (according to Eurostat, 65.9 % of all Latvian residents, and even 88.1 % in cities [3], thus sustainable planning for managing MARH is considered to be a significant spotlight at both national and local levels.

For a given moment, only a small proportion of residential houses comply with modern energy efficiency requirements, so it is necessary to take measures to encourage renovation of these buildings.

In order to improve the situation in the MARH management and reduce its negative impact on climate changes, the CLIMA project – From Housing Manager to CLImate Manager is being implemented from October 2020 to March 2023 within the framework of the European Climate Initiative (EUKI) programme. The EUKI is a project with a financing instrument by the German Federal Ministry for the Environment, Nature Conservation and Nuclear Safety (BMU).

The project participants are:

- Energy Conservation Foundation (FPE) – leading partner, Poland;
- Housing Initiative for Eastern Europe (IWO) – project partner, Germany;
- Riga Technical University (RTU) – project partner, Latvia.

Latvian state institutions (the Ministry of Economics, the Ministry of Environmental Protection and Regional Development, the State Construction Control Bureau), financial institutions (Altum) and housing managers themselves (the Association of Management and Administration of Latvian Housing (AMALH) recognise the need to accelerate the renovation of multi-apartment residential buildings by performing energy efficiency increase measures as one of the main components of climate change policy. The project therefore aims to promote the implementation of EU directives on residential renovation by developing and improving the study course programme for housing managers with climate change competences.

Accelerating the process of renovation of multi-apartment buildings requires special attention, support provided, as well as the necessary knowledge. The way to do this is to involve housing managers responsible for managing buildings in the process. However, these housing managers often lack the necessary knowledge and skills to launch and implement such projects. In order to address these shortcomings in Germany, the European Climate Initiative EUKI has already funded the KLIMAVERWALTER project, within the framework of which an innovative training scheme for acquiring the necessary skills by residential house managers has been developed

and introduced. In the CLI-MA project, a new approach is planned to the transfer of knowledge from Germany, adapting it to the specific circumstances of Latvia.

2. MANAGEMENT OF MULTI-APARTMENT RESIDENTIAL HOUSES

The housing policy, as well as matters regarding the management of multi-apartment residential buildings in Latvia are under the responsibility of the Ministry of Economics. The goal of the housing policy is to promote the quality and accessibility of housing by providing the regulatory base for the efficient management of residential buildings, by facilitating the establishment of a rental residential fund in municipal areas and by supporting energy-saving measures in residential buildings [4]. As for 1 January 2020, the monitoring and control in the field of energy, including the administration of energy efficiency issues, shall be performed by the State Construction Control Bureau.

In total in Latvia, as of the beginning of 2021, there were 366 532 residential buildings, of which 39 426 were three- or more apartment buildings [5]. The highest proportion – 85.2 % is for single-apartment or two-apartment buildings, i.e., 3.8 %, while three- and more apartment buildings make up 10.8 % of the total number.

The total area of residential buildings is 91.1 million m^2. When providing a breakdown by area (see Fig. 1), the largest proportion – 56.6 % is for three- and more apartment buildings, single-apartment buildings take up 40.1 % of the total area of residential buildings, and two-apartment buildings and social group houses constitute 3.3 %.

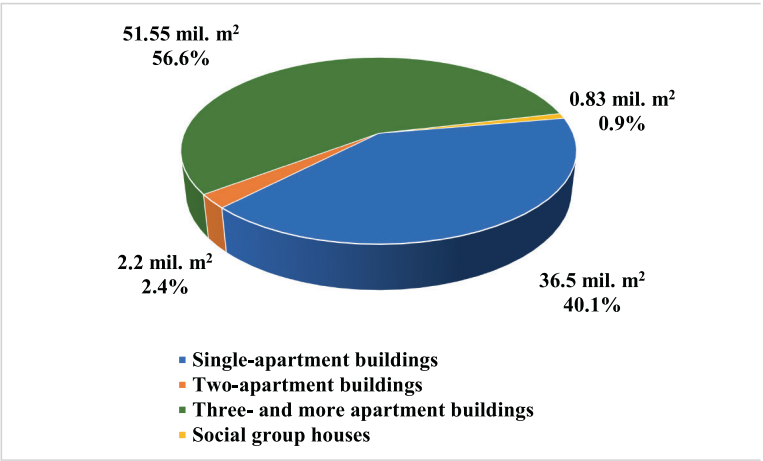

Fig. 1. Breakdown of residential buildings by area (mil. m^2) [6].

When analysing multi-apartment residential buildings by their construction year (Table 1), the bulk of them (44.6 %) were built until 1941; 13.6 % of all residential buildings were constructed between 1941 and 1960; while the most houses (24.4 %) were built during the post-war years in 1961–1979. A further 13 % of buildings were built between 1980 and 1992. However, buildings constructed after 1992 and the recovery of independence make up just 4.4 % of the number of all residential buildings.

Table 1. Breakdown of Buildings by Number of Floors and their Construction Year [6]

Houses/ Years	**Until 1941**	**1941–1960**	**1961–1979**	**1980–1992**	**1993–2002**	**2003–2014**	**2015–2019**	**Total**
Multi-apartment buildings with outer walls of wood	8622	1472	472	77	20	34	7	**10704**
Multi-apartment 1–2-storey buildings	5257	2833	3057	638	91	226	26	**12128**
Multi-apartment 3–5-storey buildings	2644	918	5350	3385	243	597	63	**13200**
Multi-apartment 6–9-storey buildings	674	32	361	657	52	195	36	**2007**
Multi-apartment buildings of 10 storeys and more	0	0	172	264	23	72	9	**540**
Total	**17197**	**5255**	**9412**	**5021**	**429**	**1124**	**141**	**38579**
Proportion, %	**44.6%**	**13.6%**	**24.4%**	**13.0%**	**1.1%**	**2.9%**	**0.4%**	**100.0%**

A majority of residential buildings have been operated for a considerable period of time, which means the necessity of gradual renovation of these buildings, while also improving their energy efficiency. In addition, the current depreciation of residential and non-residential buildings should be emphasised. According to the data provided by the State Land Service, the percentage of the total depreciation of residential houses is 38.9 %, while the depreciation of non-residential buildings is 41 % [6].

Until 1991, residential houses were built in accordance with the USSR construction standard "Thermotechnics of Building Envelopes" [6]. Construction of standard multi-apartment residential buildings was suspended after 1992. On 12 September 1991, Order No 68 of the Ministry of Architecture and Construction of the Republic of Latvia was issued on strengthening of requirements to building enclosure structures. In 2003, the construction standard LBN 002-01 "Thermotechnics of Building Envelopes" came into force, which imposed significantly stricter requirements for building enclosure structures.

In 2015, LBN 002-15 "Thermotechnics of Building Envelopes" (amendment LBN 002-01) entered into force. The amendments introduced even more stringent thermotechnical requirements to building envelopes. On 11 November 2015, amendments were made to Cabinet Regulation No. 383 of 9 July 2013 "On the Energy Certification of Buildings", which set the minimum level of energy consumption for heating, both for renewable/reconstructable buildings and new ones, as well as requirements for the gradual transition of new buildings to nearly zero-energy buildings. Consequently, new requirements were created for the construction of buildings, as well as for reconstruction and renovation projects.

In 2020, the next amendments to the construction standard LBN 002-19 "Thermotechnics of Building Envelopes" came into force, which stipulated that all new residential buildings should have to be nearly zero-energy buildings as of 2021 [7]. In 2021, the Methods for Calculating the Energy Efficiency of Buildings and Energy Certification Regulations for Buildings were adopted, which replaced the Cabinet Regulations "On the Energy Certification of Buildings" and the "Method for Calculating the Building Energy Efficiency" [8]. The requirements of all these regulatory enactments are derived from Directive (EU) 2018/844 of the European Parliament and of the Council of 30 May 2018 amending Directive 2010/31/EU on the energy effi-

ciency of buildings and Directive 2012/27/EU on energy efficiency.

The final consumption of energy resources in Latvia in 2019 was 174.8 PJ. Households consumed 49.7 PJ, corresponding to 28.5 % of the total final consumption [9]. Over the past 10 years, households have consumed 28–34 % of the total national energy consumption, so the building sector has considerable potential to achieve the overall energy efficiency targets.

According to the State Construction Control Bureau, the average specific energy consumption for heating in multi-apartment buildings was 124 kWh/m^2 per year in 2020 and 125 kWh/m^2 per year in 2019 [10]. By 2030, Latvia has committed to ensuring a reduction in the average specific thermal energy consumption in buildings to 120 kWh/m^2/year [11]. According to the Ministry of Economics, more than 23 000 buildings (in the multi-apartment building sector) would need to be renovated at the moment, but only 4 % of these buildings have actually been renovated.

From 2021 onwards, the minimum level for energy efficiency of new buildings must comply with the requirements of a nearly zero-energy building (the average specific energy consumption of a residential building for heating is not more than 40 kWh/m^2 per year); for renovated and reconstructed multi-apartment buildings, the average specific energy consumption for heating must not exceed 80 kWh/m^2 per year [7].

The Ministry of Economics states that the main problems in energy efficiency of buildings are:

- an outdated housing fund, including a low level of energy efficiency;
- low public activity and lack of interest in increasing building energy efficiency measures (bureaucratic procedures, low solvency);
- lack of information and insufficient level of education regarding the organisation and performance of energy efficiency measures for buildings;
- insufficient involvement of private investment (mostly EU structural funds and state funding are used) [6].

It can be concluded that multi-apartment residential buildings represent a significant part of the total residential area in Latvia, and most of these buildings have high energy consumption and significantly lower thermal performance than can be provided with currently available technologies [11].

3. RESULTS AND DISCUSSION

According to the Law on Administration of Residential Houses, each residential house must be ensured that it is properly operated, maintained and improved, as well as its continuous management process. A person is entitled to perform an administrative task in a multi-apartment building when having acquired the vocational education required for the management of residential buildings and a specified level of professional qualification.

Such an administrator should also plan energy efficiency improvement measures, including replacing depreciated elements or constructions, where the average thermal energy consumption of the building used for heating the building exceeds 150 kWh/m^2 per year over the last three calendar years.

In order to clarify the opinion of current and potential employees in this sector, a survey was conducted regarding what skills, if any, are needed for a house administrator on

energy efficiency of buildings and climate change issues.

The survey questions covered the following aspects:

- the experience and plans of respondents with regard to the implementation of measures to improve the energy performance of buildings;
- self-assessment of respondents as regards their competences for the implementation of energy efficiency measures for buildings;
- views of respondents on a complex approach to the implementation of measures to improve the energy performance of buildings related to the interaction between different aspects of the management of non-residential properties (technical, legal, financial, organisational, social, information exchange, etc.);
- the need for specific skills and competences in the planning and implementation of technical, legal, financial, organisational, social, information exchange and other issues.

The survey involved 63 respondents, namely:

- members of the Association of Management and Administration of Latvian Housing (the Association of Management and Administration of Latvian Housing is a public organisation uniting natural and legal persons throughout the Republic of Latvia who are interested in achieving common objectives in the administration and management of real estate[12]),
- future housing managers studying at Riga Technical University.

A majority of the respondents (86 %) believe that in the future they will have to deal with the organisation of energy efficiency measures in buildings with a high probability (Fig. 2).

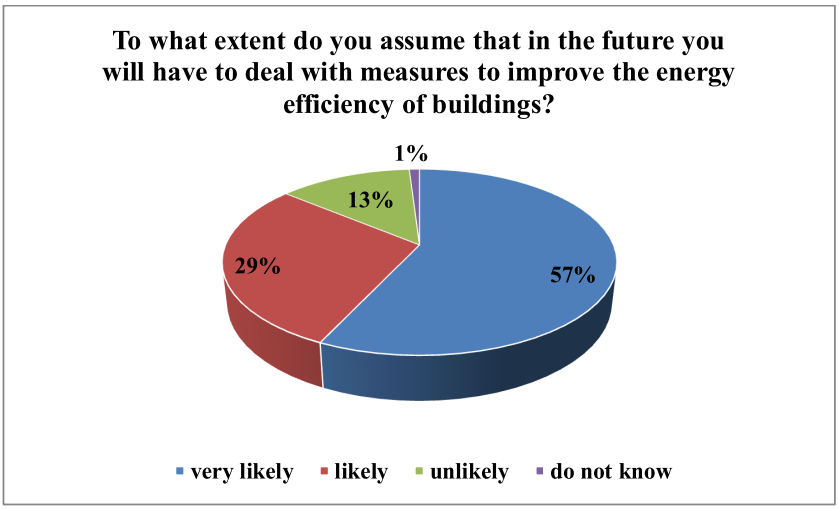

Fig. 2. Plans of respondents.

It should be noted that 39 % of those surveyed have already participated in implementing energy efficiency measures at least once. Yet, more than 60 % have never come across it (Fig. 3).

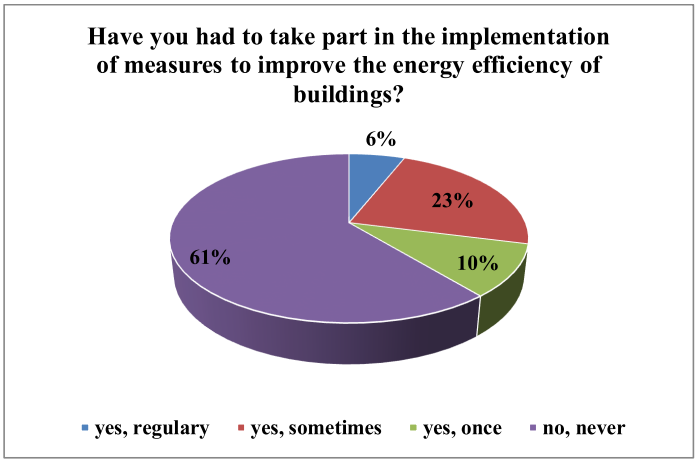

Fig. 3. Experience of respondents.

Assessing their competences in the implementation of energy efficiency measures regarding financing issues, technical solutions, legal issues, organisational aspects and promotion of energy efficiency measures (Fig. 4), on average 15–30 % respondents consider them to be of high or sufficient qualifications, while 50–70 % consider their knowledge to be partial or insufficient. According to the survey, 10–20 % have self-assessment problems. The lowest level of assessment of existing competence is in the legal sphere, as well as in the search for technical and financing solutions.

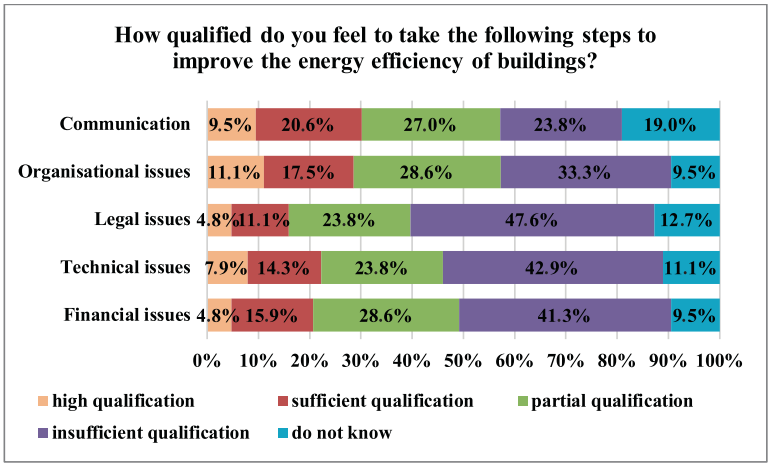

Fig. 4. Self-assessment of respondents.

All respondents (95 % fully and 5 % partially) agree with the statement that the successful implementation of energy efficiency measures for buildings requires interaction between the various aspects of real estate management (technical, legal, financial, organisational, social, information exchange, etc.).

As far as technical knowledge is concerned, a convincing majority (82–92 % fully and about 6–16 % partially; 98 % in total) consider that successful implementation of measures to improve the energy efficiency of buildings requires knowledge and skills on at least the following issues:

- Building microclimate;
- Construction physics of building structures;
- Energy efficiency of building envelopes;
- Energy efficiency of engineering communications of buildings;
- Energy efficient building materials.

Regarding issues on financial and economic knowledge, 70–80 % fully and 16–27 % partly agree that the successful implementation of measures to increase energy efficiency of buildings requires at least the following:

- Investment in energy efficiency measures;
- Financial support instruments for energy efficiency measures;
- Economic evaluation of energy efficiency projects;
- Basic principles for setting up service tariffs.

70–80 % fully and 18–29 % partly agree that successful implementation of energy efficiency measures for buildings requires legal expertise on at least the following issues:

- the regulatory framework for energy efficiency and renewable energy;
- the regulatory framework for the construction processes;
- the regulatory framework for the administration of buildings;
- construction contracts;
- contracts on services (heating, water supply, electricity supply, etc.).

80–94 % fully and 5–19 % partly agree that the successful implementation of energy efficiency measures for buildings requires organisational and management skills:

- in project management;
- in risk management;
- in planning energy efficiency and renewable energy measures.

Regarding communication skills, 83 % of respondents fully and 17 % partially acknowledge that minimum the following is needed:

- holding negotiations and meetings;
- solution of conflicts;
- cooperation;
- consultation;
- speeches and presentations.

Having summarised all of the obtained results, it can be concluded that:

1. The qualifications of existing and future housing managers are not sufficient and additional knowledge needs to be acquired;
2. The successful implementation of energy efficiency measures for buildings requires competences in different aspects of the administration of non-residential properties (technical, legal, financial, organisational, social, information exchange, etc.), and therefore training should be developed to cover all these issues.

The knowledge required for housing managers to perform their duties and tasks by categories is provided in Fig. 5.

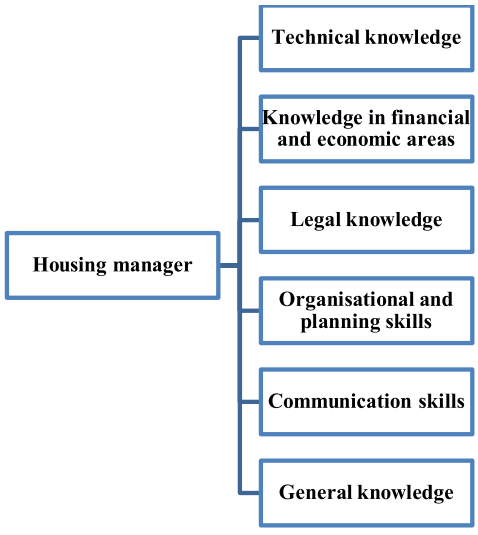

Fig. 5. Categories of required knowledge.

In order to establish a high-quality and comprehensive programme for such training, it is necessary to develop a description of a housing manager with competence for climate change mitigation, including a description of the activities of the housing manager, key responsibilities and tasks, as well as the necessary skills, attitudes and resources to fulfil them. Having clarified the above issues, it is possible to define the necessary knowledge and competences for the successful performance of job responsibilities and tasks and to develop the necessary skills.

The methodology for the characterisation of the housing manager with competence to mitigate climate change is based on the structure of qualifications for the real estate management sector and complies with the Methodology for Developing the Requirements for Occupational Standards/Professional Qualification [13]. The description of the housing manager includes the following sections:

1. Brief activity description;
2. Basic duties;
3. Main tasks;
4. Skills required to fulfil basic duties and tasks
5. Knowledge (general and professional);
6. Required competences.

Schematically, the process of determining the required competences of housing manager is provided in Fig. 6.

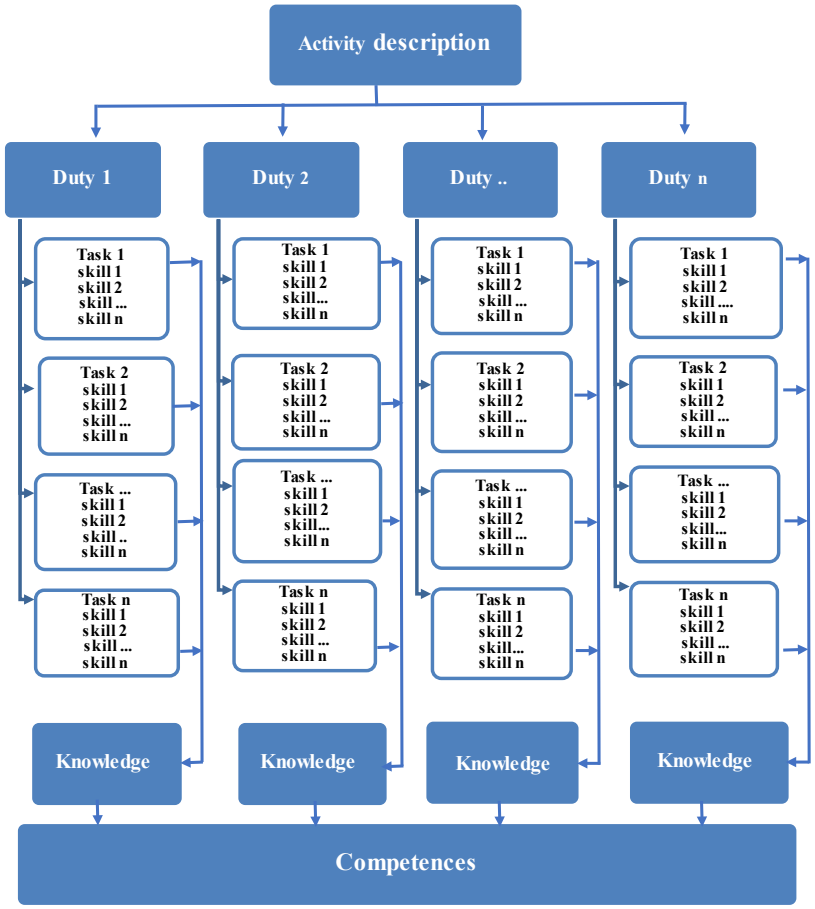

Fig. 6. Methodology for determining the required competences.

The activity description provides information on the mission, key responsibilities, the environment in which the professional representative operates and the degree of responsibility.

Other characterising elements are defined below [13]:

- The obligation is a long-term work, which is a grouping of related tasks, which has no set start and end and which is difficult to measure.
- The task is a completed, measurable unit of work which ensures that an obligation is fulfilled in general.
- Skill is the ability to perform an activity according to the quality and extent required, and is a prerequisite for performance.
- Knowledge – a systematised set of objective concepts obtained through learning, work experience, research and the like; it results from cognition.
- Competence – the necessary knowledge, professional experience, awareness in a specific field, issue and skills to use knowledge and experience in a specific activity.

4. CONCLUSIONS

One of the problems identified in the policy documents developed by the Ministry of Economics (Latvian National Energy and Climate Plan for 2021–2030, the Long-term Strategy for Renewal of Buildings) in the field of energy efficiency of buildings in Latvia is an insufficient level of education regarding the organisation and performance of energy efficiency improvement measures for buildings.

The results of the survey conducted within the framework of the research confirm this statement, since the majority of respondents consider that the qualifications of housing managers are insufficient at the moment and that additional knowledge is needed.

In order to achieve the objectives set out in the Latvian development planning documents in the field of energy efficiency of buildings, the duly educated housing managers with competence in energy efficiency and climate change issues are required, who would be able to organise the implementation of energy efficiency measures and the appropriate maintenance of buildings after taking such measures.

The identification of the required competences requires the development of a description of the specific profession, including a description of the activities of the housing manager, the main duties, tasks and the necessary skills to further define the required knowledge and competences.

For the successful implementation of energy efficiency measures for buildings, housing managers need competence in technical, legal, financial, organisational, social, information exchange and other issues. The acquisition of these competences should constitute a training course programme covering all these aspects.

ACKNOWLEDGEMENTS

This research has been funded by the project “From Housing Manager to CLImate Manager”. This project is part of the European Climate Initiative (EUKI). EUKI is a project financing instrument by the German Federal Ministry for the Environment,

Nature Conservation and Nuclear Safety (BMU). The EUKI competition for project ideas is implemented by the Deutsche Gesellschaft für Internationale Zusammenarbeit (GIZ) GmbH. It is the overarching goal of the EUKI to foster climate cooperation within the European Union (EU) in order to mitigate greenhouse gas emissions. Agreement number: 81263938, Project processing number: 17.9045.0-002.77

REFERENCES

1. Geipele, I., Kundziņa, A., Zvirgzdiņš, J., Pļaviņa, B., & Stāmure, I. (2021). *Market research among facility managers, public bodies and financing institutions in Latvia regarding the scope of existing and required skills of building managers on topics related to mitigation of climate change caused by buildings in Latvia*. Riga: RTU.
2. Saeima. (2020). *Latvian National Development Plan for 2021–2027 (NAP2027)*. Available at https://likumi.lv/ta/id/315879-par-latvijas-nacionalo-attistibas-planu-20212027-gadam-nap2027
3. Eurostat. (2021). *House or Flat – Owning or Renting*. Available at https://ec.europa.eu/eurostat/cache/digpub/housing/bloc-1a.html?lang=en
4. Ministry of Economics. (n.d.). *Housing*. Available at *https://www.em.gov.lv/en/housing*
5. Valsts zemes dienests. (2021). *Reģistrēto būvju skaits sadalījumā pa galvenajiem lietošanas veidiem*. Available at https://www.vzd.gov.lv/lv/registreto-buvju-skaits-sadalijuma-pa-galvenajiem-lietosanas-veidiem
6. Ministry of Economics. (2020). *Informative Report "Long-term Strategy for Building Renovation"*. Available at http://tap.mk.gov.lv/mk/tap/?pid=40487380
7. Cabinet Regulation No 280. (2019). *Regulation on Latvian Construction Standard LBN 002-19 "Thermotechnics of Building Envelopes"*. Available at https://likumi.lv/ta/id/307966-noteikumi-par-latvijas-buvnormativu-lbn-002-19-eku-norobezojoso-konstrukciju-siltumte
8. Cabinet Regulation No 222. (2021). *Ēku energoefektivitātes aprēķina metodes un ēku energosertifikācijas noteikumi*. Available at https://likumi.lv/ta/id/322436-eku-energoefektivitates-aprekina-metodes-un-eku-energosertifikacijas-noteikumi
9. Official statistical portal. (2020). *Latvijas energobilance 2019. gadā*. Available at https://admin.stat.gov.lv/system/files/publication/2020-08/Nr_23_Latvijas_energobilance_2019_gada_%2820_00%29_LV.pdf
10. Būvniecības valsts kontroles birojs. *(2021). Vidējais energoefektivitātes rādītājs*. *Available at* https://www.bvkb.gov.lv/lv/energoefektivitates-jautajumu-administresana
11. Cabinet Order No 46. (2020). *Latvijas nacionālais enerģētikas un klimata plāns 2021. – 2030. gadam*. Available at https://likumi.lv/ta/id/312423-par-latvijas-nacionalo-energetikas-un-klimata-planu-20212030-gadam
12. Association of Management and Administration of Latvian Housing. (2021). Available at http://www.lnpaa.lv
13. Valaine, S., Kaukule, H., Daņilova, T, Annuškāne, I., Vīgante, D., Strode, L.I., & Braunšteins, B. (2017). *Profesiju standartu /profesionālās kvalifikācijas prasību izstrādes metodika*. Riga: National Centre for Education.

sciendo

LATVIAN JOURNAL OF PHYSICS
AND TECHNICAL SCIENCES
2021, N 6

DOI: 10.2478/lpts-2021-0045

INVESTIGATION OF THE FLOW-BASED FAST REROUTE MODEL WITH IMPLEMENTATION OF A MULTIMEDIA QUALITY PROTECTION SCHEME

O. Lemeshko[1], M. Yevdokymenko[2], O. Yeremenko[3],
N. Kunicina[4], A. Ziravecka[5]

[1–3] V.V. Popovskyy Department of Infocommunication Engineering,
Kharkiv National University of Radio Electronics
14 Nauky Ave., Kharkiv, 61166, UKRAINE
[4,5] Riga Technical University
12/1 Azenes Str., Riga, LV-1048, LATVIA
E-mail: [1]oleksandr.lemeshko.ua@ieee.org,
[2]maryna.yevdokymenko@ieee.org,
[3]oleksandra.yeremenko.ua@ieee.org,
[4]nadezda.kunicina@rtu.lv,
[5]anastasija.ziravecka@rtu.lv

In this paper, a tensor flow-based fast reroute model with multimedia quality protection is proposed. In the model, the conditions for implementing a multipath routing strategy and flow conservation are introduced taking into account possible packet loss at the network nodes and preventing overloading communication links both when using the primary and backup routes. At the same time, the novelty of the proposed solution is the formalization of the conditions of protection of the Quality of Experience level in terms of multimedia quality along the primary and backup routes. These conditions have been obtained during the tensor formalization of the network, which made it possible to calculate the quality of service indicators: packet loss probabilities, as well as the average end-to-end delay for audio and video flows transmitted in the multimedia session using the primary and backup routes, respectively. As a criterion for the optimality of the obtained solutions, a condition has been selected related to maximizing the overall performance of the infocommunication network. The results of the research of the proposed model confirm the adequacy of the numerical research results obtained for solving the problem of fast rerouting with link/node protection.

Keywords: *Average end-to-end delay, fast rerouting, multimedia quality, packet loss probability, quality of experience, tensor.*

1. INTRODUCTION

At this stage in the development of infocommunication networks (ICNs), one of the most important requirements put forward by them is to ensure a high level of fault tolerance solutions while maintaining the Quality of Service (QoS). The analysis shows that in practice several approaches are implemented [1]–[10], which are mainly aimed at ensuring either network fault tolerance [1]–[3] or supporting a high level of QoS [4]–[10]. The demand for complex solutions in this area is especially relevant when transmitting multimedia traffic, the volume of which is rapidly growing in modern ICNs.

One of the most effective technological means of ensuring network resiliency is the Fast ReRouting (FRR) protocols [7]–[14]. They should provide a real-time response to possible failures of network equipment based on preliminary calculation and subsequent use of many primary and backup routes with the implementation of local and global protection schemes – a node, link or route. At the same time, it is very important, along with the reservation of its structural elements, to provide protection of the main QoS indicators. Therefore, for example, the works [14]–[16] are devoted to the development of solutions for protecting network bandwidth, and in articles [17]–[22] models and methods are aimed at protecting numerical values of multiple end-to-end QoS indicators simultaneously – bandwidth, average delay, packet loss.

However, when transmitting multimedia traffic, for example, voice or online video, it is rather difficult to assess the efficiency of the distribution of network resources and the QoS in the ICN at the end-user level. One way to evaluate QoS for a number of multimedia applications, according to ITU-T [23], [26]–[28], is Mean Opinion Score (MOS), which determines the Quality of Experience (QoE) at the user level. These QoE indicators, taking into account the characteristics of the network, the types of end equipment on the client side, the characteristics of the transmitted multimedia traffic, allow for a more adequate assessment of the quality of the provided multimedia service.

Providing the specified values of QoE indicators using routing tools is a rather complicated scientific and applied problem, requiring a review of not only the relevant protocols but also the mathematical models and methods underlying them, as well as computational algorithms. In this regard, in this paper, the main attention will be paid to the development of an approach that allows, under the conditions of fast rerouting, providing the specified values of QoE indicators along with both the primary and backup routes.

2. FLOW-BASED FAST REROUTE MODEL WITH PROTECTION OF MILTIMEDIA QUALITY LEVEL IN THE INFOCOMMUNICATION NETWORK

To protect the level of multimedia quality in conditions of fast rerouting in the ICN, the flow-based model [24] is used. Here the network structure is presented using a one-dimensional simplicial complex $S = (U, V)$ where

$U = \{u_i, i = \overline{1,m}\}$ is a set of zero-dimensional simplexes – network nodes (routers) and $V = \{v_z = (i,j);\ z = \overline{1,n};\ i,j = \overline{1,m};\ i \neq j\}$ is a set of one-dimensional simplexes – network links where the link $v_z = (i,j)$ models the z-th link that connects the routers u_i and u_j. For each link modelled by the edge $v_z = (i,j) \in V$, the bandwidth will be denoted both through φ_z and $\varphi_{i,j}$ (1/s). Each network router has several interfaces through which it sends packets to its neighbouring nodes. Then $\varphi_{i,j}$ actually determines the bandwidth of the j-th interface of the i-th node.

Further, we assume that K denotes a set of multimedia sessions on the ICN. Then to solve the QoE-FRR problem, it is necessary to calculate a set of routing variables:

- $x_{i,j}^{k^{sp}}$ and $x_{i,j}^{k^{video}}$, each characterises the fraction of the rate of the audio and video flows generated during the k-th multimedia session and flow in the link (i,j) belonging to the primary route, respectively;
- $\overline{x}_{i,j}^{k^{sp}}$ and $\overline{x}_{i,j}^{k^{video}}$ are the fractions of the rate of the audio and video flows generated during the k-th multimedia session and flow in the link (i,j) belonging to the backup route, respectively.

Then when using a multipath routing strategy, the next limitations are imposed on routing variables:

$$\begin{cases} 0 \le x_{i,j}^{k^{sp}} \le 1, \\ 0 \le x_{i,j}^{k^{video}} \le 1. \end{cases} \text{ and } \begin{cases} 0 \le \overline{x}_{i,j}^{k^{sp}} \le 1, \\ 0 \le \overline{x}_{i,j}^{k^{video}} \le 1. \end{cases} \quad (1)$$

To account for possible packet loss caused by overloading the queue buffer on the network nodes, the conditions for conservation of audio and video flows for the primary route takes the following form [24]:

$$\begin{cases} \sum\limits_{j:(i,j)\in V} x_{i,j}^{k^{sp}} = 1 \ \text{ if } \ k^{sp} \in K,\ u_i = b_k; \\ \sum\limits_{j:(i,j)\in V} x_{i,j}^{k^{sp}} - \sum\limits_{j:(j,i)\in V} x_{j,i}^{k^{sp}} (1 - p_{j,i}) = 0 \ \text{ if } \ k^{sp} \in K,\ \ u_i \neq b_k, u_i \neq d_k; \\ \sum\limits_{j:(j,i)\in V} x_{j,i}^{k^{sp}} (1 - p_{i,j}) = \varepsilon^{k^{sp}} \ \text{ if } \ k^{sp} \in K,\ \ u_i = d_k, \end{cases} \quad (2)$$

$$\begin{cases} \sum\limits_{j:(i,j)\in V} x_{i,j}^{k^{video}} = 1 \ \text{ if } \ k^{video} \in K,\ u_i = b_k; \\ \sum\limits_{j:(i,j)\in V} x_{i,j}^{k^{video}} - \sum\limits_{j:(j,i)\in V} x_{j,i}^{k^{video}} (1 - p_{j,i}) = 0 \ \text{ if } \ k^{video} \in K,\ \ u_i \neq b_k, u_i \neq d_k; \\ \sum\limits_{j:(j,i)\in V} x_{j,i}^{k^{video}} (1 - p_{i,j}) = \varepsilon^{k^{video}} \ \text{ if } \ k^{video} \in K,\ \ u_i = d_k, \end{cases} \quad (3)$$

where b_k is the source router and d_k is the destination router for packets of audio and video flows of the k-th multimedia session, respectively; $\varepsilon^{k^{sp}}$ and $\varepsilon^{k^{video}}$ are the fractions of rate of the audio flow k^{sp} and video flow k^{video} serviced by the network, i.e., packets of which have been successfully delivered to the destination router; $p_{i,j}$ is the probability of packet loss on the j-th interface of the i-th router.

The conditions for conservation of audio and video flows for the backup route have a similar form (2) and (3), where $\overline{p}_{i,j}^{k}$ is the probability of packet loss on the j-th interface of the i-th router, which is included in the backup path. The probability of packet loss traditionally depends on the characteristics of the traffic, the discipline of their service, and the state of the interface. The probability of packet loss, if the j-th interface of the i-th router is modelled by a queuing system with failures of the type, for example, $M/M/1/N$, can be calculated as follows:

$$p_{i,j}=\frac{\left(1-\rho_{i,j}\right)\left(\rho_{i,j}\right)^{N_{i,j}}}{1-\left(\rho_{i,j}\right)^{N_{i,j}+1}} \quad \text{and} \quad \overline{p}_{i,j}=\frac{\left(1-\overline{\rho}_{i,j}\right)\left(\overline{\rho}_{i,j}\right)^{N_{i,j}}}{1-\left(\overline{\rho}_{i,j}\right)^{N_{i,j}+1}}\ , \tag{4}$$

where $\rho_{i,j}=\frac{\lambda_{i,j}}{\varphi_{i,j}}$ and $\overline{\rho}_{i,j}=\frac{\overline{\lambda}_{i,j}}{\varphi_{i,j}}$ are the utilization coefficients of the j-th interface on the i-th router, which is included in the primary and backup paths, respectively; $N_{i,j}$ denotes the maximum number of packets in the queue of the j-th interface on the i-th router; $\varphi_{i,j}$ denotes the bandwidth of the j-th interface of the i-th router, measured in 1/s; $\lambda_{i,j}$ and $\lambda_{i,j}$ are the total rate of all flows of various multimedia sessions in the link $(i,j)\in V$ (1/s) belonging to the primary or backup routes, respectively, calculated using the expression

$$\begin{cases}\lambda_{i,j}=\sum\limits_{k\in K}\left(\lambda^{k^{sp}}x_{i,j}^{k^{sp}}+\lambda^{k^{video}}x_{i,j}^{k^{video}}\right)\\ \overline{\lambda}_{i,j}=\sum\limits_{k\in K}\left(\overline{\lambda}^{k^{sp}}\overline{x}_{i,j}^{k^{sp}}+\overline{\lambda}^{k^{video}}\overline{x}_{i,j}^{k^{video}}\right)\end{cases}, \tag{5}$$

where $\lambda^{k^{sp}}$ and $\lambda^{k^{video}}$ are the average packet rates of the audio and video flows of the k-th multimedia session, respectively, generated along the primary path; $\overline{\lambda}^{k^{sp}}$ and $\overline{\lambda}^{k^{video}}$ are the average packet rates of the audio and video flows of the k-th multimedia session, respectively, generated along the backup path. The rates of successfully transmitted packets of audio $\lambda_{i,j}^{k^{sp}}$ and video $\lambda_{i,j}^{k^{video}}$ flows of the k-th multimedia session through the j-th interface of the i-th router belonging to the primary route, are calculated as follows:

$$\lambda_{i,j}^{k^{sp}}=\lambda^{k_{sp}}x_{i,j}^{k^{sp}}\left(1-p_{i,j}\right); \tag{6}$$

$$\lambda_{i,j}^{k^{video}}=\lambda^{k_{video}}x_{i,j}^{k^{video}}\left(1-p_{i,j}\right). \tag{7}$$

The rate of successfully transmitted packets of audio $\overline{\lambda}_{i,j}^{k^{sp}}$ and video $\overline{\lambda}_{i,j}^{k^{video}}$ flows of the k-th multimedia session through the j-th interface of the i-th router belonging to the backup route is calculated in similar form as (6) and (7).

To ensure control over the process of overloading links and queues when using the primary and backup routes, taking into account Eq. (5), the following restrictions are introduced into the model structure [24]:

$$\lambda_{i,j}<\varphi_{i,j} \text{ and } \overline{\lambda}_{i,j}<\varphi_{i,j} \text{ under } (i,j)\in V. \tag{8}$$

3. CONDITIONS FOR PROTECTION MULTIMEDIA QUALITY IN THE IMPLEMENTATION OF FAST REROUTING

The main requirement when implementing fast rerouting is to meet the conditions for ensuring a given level of MultiMedia Quality. In accordance with the ITU-T Recommendation G.1070 [19], the requirements for MultiMedia Quality (MM_q) along primary and backup routes, respectively, are generally defined as follows:

$$MM_q \geq MM_q^{<req>}, \quad \text{at } 1 \leq MM_q \leq 5. \tag{9}$$

$$\overline{MM_q} \geq MM_q^{<req>}, \quad \text{at } 1 \leq \overline{MM_q} \leq 5, \tag{10}$$

where

$$MM_q = m_1 MM_{SV} + m_2 MM_T + m_3 MM_{SV} MM_T + m_4, \tag{11}$$

$$\overline{MM_q} = m_1 \overline{MM_{SV}} + m_2 \overline{MM_T} + m_3 \overline{MM_{SV}}\,\overline{MM_T} + m_4, \tag{12}$$

where $MM_q^{<req>}$ is the requirement for the MultiMedia Quality level; MM_{SV} and $\overline{MM_{SV}}$ are the quality of transmission of audiovisual information along primary and backup routes, respectively; MM_T and $\overline{MM_T}$ denote degradation in quality due to delays and desynchronization of processes for transmitting audio and video flow packets along primary and backup routes, respectively; m_i – coefficients depending on the size of the display and the purpose of communication [23], [24].

The main difficulty in ensuring the set values of QoE indicators during fast rerouting was the need for analytical calculation of indicators MM_q and $\overline{MM_q}$ in order to fulfill conditions (9) and (10) for each multimedia session generated along the primary and the backup routes, respectively. At the same time, in order to calculate these indicators MM_q and $\overline{MM_q}$ in the framework of a multimedia session when transmitting packets of audio and video flows along the primary and backup routes, it is necessary to calculate the terms presented in accordance with the methodology described in ITU-T G.1070.

Moreover, the terms included in (11) and (12), as well as the transmission quality of audio (S_q), ($\overline{S}_q$) and video flows (V_q), ($\overline{V}_q$), are the functions of the average end-to-end delays of packets of audio (T_S), ($\overline{T}_S$) and video (T_V), ($\overline{T}_V$) flows, the probabilities of packet losses of audio (P^S), ($\overline{P}^S$) and video (P^V), ($\overline{P}^V$) flows along primary and backup routes, respectively, and are determined in accordance with the recommendation [11]. In other words, when transmitting a multimedia flow along the primary route, the transmission quality of audiovisual information MM_{SV} is determined using the following expressions:

$$MM_{SV} = m_5 S_q + m_6 V_q + m_7 S_q V_q + m_8, \text{ at } 1 \le MM_{SV} \le 5, \tag{13}$$

$$MM_T = \max\{AD + MS, 1\}, \text{ at } 1 \le MM_T \le 5, \tag{14}$$

$$AD = m_9(T_S + T_V) + m_{10}, \tag{15}$$

$$MS = \begin{cases} \min\left[m_{11}(T_S - T_V) + m_{12},\ 0\right], & \text{if } T_S \ge T_V, \\ \min\left[m_{13}(T_V - T_S) + m_{14},\ 0\right], & \text{if } T_S < T_V, \end{cases} \tag{16}$$

where MS is the coefficient that takes into account the desynchronization between the audio and the video; AD is the parameter reflecting the effect of average delays of packets of audio (T_S) and video (T_V) flows. Then, in accordance with recommendation [23], the presented expressions, in this case similar to (13)–(16), can be used to form restrictions of Eq. (9) based on the known required level of quality of multimedia traffic $MM_q^{<req>}$ transmitted along the primary path. When using the backup route during the transmission of a multimedia flow, expressions similar to (13)–(16) will be used to calculate $\overline{MM}_{SV}$ and $\overline{MM}_T$.

The main problem in the calculation MM_q and $\overline{MM}_q$ is the definition of expressions for finding the values of the end-to-end delays, as well as the packet loss probabilities for audio and video flows (Table 1), transmitted along the primary or backup paths. This is due to the fact that these indicators directly depend on route variables (1), traffic characteristics and network parameters. Therefore, based on the model (1)–(6), the expressions for calculation of P^S, $\overline{P}^S$ and P^V, $\overline{P}^V$ will take the form:

$$P^S = 1 - \varepsilon^{k^{sp}}, \quad \overline{P}^S = 1 - \overline{\varepsilon}^{k^{sp}}, \tag{17}$$

$$P^V = 1 - \varepsilon^{k^{video}}, \quad \overline{P}^V = 1 - \overline{\varepsilon}^{k^{video}}. \tag{18}$$

To derive analytical expressions for determining T_S, $\overline{T}_S$ and T_V, $\overline{T}_V$ taking into account the results obtained in [20], it is advisable to use the functional of tensor modelling of routing processes in infocommunication networks.

4. TENSOR FORMALIZATION FAST REROUTE MODEL IN INFOCOMMUNICATION NETWORK

In accordance with the methodology for tensor modelling of an ICN proposed in [24], [27], the network structure determines the anisotropic space formed by a set of circuits and node pairs. The dimension of this space is determined by the total number of edges (communication links) in the network and is equal to n.

Moreover, each independent path (edge, circuit, or node pair) determines the coordinate axis in the space structure. As a rule, an ICN is modelled by a connected one-dimensional network, i.e., it contains one connected component. Then the cyclomatic number μ and the rank ϕ of the network determine, respectively, the number of basic circuits and node pairs, for which the following expressions are true:

$$\mu = n - m + 1, \quad \phi = m - 1, \quad n = \phi + \mu \tag{19}$$

In the selected space when transmitting packets of each pair of audio and video flows generated during the k-th multimedia session along primary route, the infocommunication network can be represented by a mixed bivalent tensor

$$\Omega = T \otimes \Lambda, \tag{20}$$

where $\otimes$ is the tensor multiplication operator, the components of the tensor Ω are the univalent covariant tensor of average packet delays T and the univalent contravariant tensor of flow rates Λ in the coordinate paths of the network.

The average packet delay in an arbitrary ICN communication link for both audio and video flows along primary routes is approximated by the expression

$$\tau = \frac{\rho - \rho^{N+2} - (N+1)\rho^{N+1}(1-\rho)}{\lambda(1-\rho^{N+1})(1-\rho)}. \tag{21}$$

In accordance with the postulate of G. Kron second generalization [25] and the results of [14], [17], [24], Eq. (21) written for each of the network links determines the following vector-matrix equation:

$$\Lambda_v = G_v T_v \tag{22}$$

where Λ_v and T_v are the projections of the tensors Λ and T, respectively, in the coordinate systems of the edges represented by the n-dimensional vectors of the flow rate and average packet delay in the communication links belonging to the primary routes; $G_v = \left\| g_v^{ij} \right\|$ is a diagonal $n \times n$ matrix, the elements of which corresponded to the edges (links) of the network and calculated as an example of servicing the audio flow according to Eq. [25]:

$$g_v^{ii} = \frac{\lambda_i \,(1-(\rho_i^v)^{N_i^v+1})(1-\rho_i^v)\lambda_i^v}{\rho_i^v - (\rho_i^v)^{N_i^v+2} - (N_i^v+1)(\rho_i^v)^{N_i^v+1}(1-\rho_i^v)}, \tag{23}$$

where the index i indicates the belonging of a particular interface parameter to the link $v_i \in V$; λ_i is the total rate of all flows of various multimedia sessions in the link $v_i \in V$ (5); λ_i^v denotes a packet rate of the considered audio flow in the link $v_i \in V$. The projections of the tensors of the average packet delays and flow rates in the coordinate system of the circuits and node pairs are connected by the expression similar to (22):

$$\Lambda_{\pi\eta} = G_{\pi\eta} T_{\pi\eta}. \tag{24}$$

According to the law of coordinate transformation, the tensor G is a twice contravariant metric tensor, the projections of which are transformed as follows when the coordinate system of its consideration is changed:

$$G_{\pi\eta} = A^t G_v \, A, \tag{25}$$

where $G_{\pi\eta}$ is the projection of the tensor G in the coordinate system of circuits and node pairs; A is the $n \times n$ covariant transformation matrix; $[\cdot]^t$ is the transposition operation. As shown in [17], [24], the matrix $G_{\pi\eta}$ can be represented as a block structure, i.e.:

$$G_{\pi\eta} = \left\| \begin{array}{c|c} G_{\pi\eta}^{\langle 1 \rangle} & G_{\pi\eta}^{\langle 2 \rangle} \\ \hline G_{\pi\eta}^{\langle 3 \rangle} & G_{\pi\eta}^{\langle 4 \rangle} \end{array} \right\|, \quad G_{\pi\eta}^{4} = \left\| \begin{array}{c|c} G_{\pi\eta}^{\langle 4,1 \rangle} & G_{\pi\eta}^{\langle 4,2 \rangle} \\ \hline G_{\pi\eta}^{\langle 4,3 \rangle} & G_{\pi\eta}^{\langle 4,4 \rangle} \end{array} \right\|,$$

where $G_{\pi\eta}^{\langle 1\rangle}$ and $G_{\pi\eta}^{\langle 4\rangle}$ are the square submatrices of the sizes $\mu\times\mu$ and $\phi\times\phi$, respectively; $G_{\pi\eta}^{\langle 2\rangle}$ is the submatrix of the size $\mu\times\phi$; $G_{\pi\eta}^{\langle 3\rangle}$ is the submatrix of the size $\phi\times\mu$; $G_{\pi\eta}^{\langle 4,1\rangle}$ is the first element of the matrix $G_{\pi\eta}^{\langle 4\rangle}$; $G_{\pi\eta}^{\langle 4,2\rangle}$ is the second element of the matrix $G_{\pi\eta}^{\langle 4\rangle}$ of the size $1\times(\phi-1)$; $G_{\pi\eta}^{\langle 4,3\rangle}$ is the third element of the matrix $G_{\pi\eta}^{\langle 4\rangle}$ of the size $(\phi-1)\times 1$; and $G_{\pi\eta}^{\langle 4,4\rangle}$ is the fourth element of the matrix $G_{\pi\eta}^{\langle 4\rangle}$ of the size $(\phi-1)\times(\phi-1)$.

In the framework of the tensor description of the infocommunication network in the context of the multipath routing strategy [14], [17], [24], the average end-to-end delay of the audio flow packets along the primary route can be calculated as follows:

$$T_S=\frac{\lambda^{k^{sp}}\varepsilon^{k^{sp}}-G_{\pi\eta}^{\langle 4,2\rangle}\left[G_{\pi\eta}^{\langle 4,4\rangle}\right]^{-1}\Lambda_{\eta-1}^{k^{sp}}}{\left(G_{\pi\eta}^{\langle 4,1\rangle}-G_{\pi\eta}^{\langle 4,2\rangle}\left[G_{\pi\eta}^{\langle 4,4\rangle}\right]^{-1}G_{\pi\eta}^{\langle 4,3\rangle}\right)}, \quad (26)$$

where $\Lambda_{\varsigma-1}^{k^{sp}}$ is the rate vector of lost packets on the interfaces of routers, the coordinates of which are determined by the expression:

$$\lambda_\eta^i=\sum_{j=1}^{m}\lambda^{k^{sp}}x_{i,j}^{k^{sp}}p_{i,j}. \quad (27)$$

To determine the average end-to-end delay of the video flow T_V packets for the primary route, one can use expressions similar to (26) and (27) with some correction of the metric (23), in which λ_i^v will already numerically characterize the packet intensity of the considered video flow in the link $v_i\in V$. Thus, the average end-to-end delay of video flow T_V packets along primary route is calculated as follows:

$$T_V=\frac{\lambda^{k^{video}}\varepsilon^{k^{video}}-G_{\pi\eta}^{\langle 4,2\rangle}\left[G_{\pi\eta}^{\langle 4,4\rangle}\right]^{-1}\Lambda_{\eta-1}^{k^{video}}}{G_{\pi\eta}^{\langle 4,1\rangle}-G_{\pi\eta}^{\langle 4,2\rangle}\left[G_{\pi\eta}^{\langle 4,4\rangle}\right]^{-1}G_{\pi\eta}^{\langle 4,3\rangle}}, \quad (28)$$

where $\Lambda_{\varsigma-1}^{k^{video}}$ is the intensity vector of the lost packets of the video flow on the interfaces of the routers along the primary route, the coordinates of which are determined similarly to Eq. (27).

The technique for obtaining the required conditions for ensuring the quality of service by the average end-to-end delay of audio $\overline{T}_S$ and video $\overline{T}_V$ flow packets along the backup routes is similar to that described above (19)–(28).

As a criterion for the optimality of the obtained solutions in term QoE-FRR, we selected a condition, which allowed maximizing the overall performance of the infocommunication network [24]:

$$\max_{x,\varepsilon}\sum_{k\in K}\left(\lambda^{k^{sp}}\varepsilon^{k^{sp}}+\overline{\lambda}^{k^{sp}}\overline{\varepsilon}^{k^{sp}}+\lambda^{k^{video}}\varepsilon^{k^{video}}+\overline{\lambda}^{k^{video}}\overline{\varepsilon}^{k^{video}}\right) \quad (29)$$

in the presence of restrictions (1), (2), (5), (9), considering their detail in (10)–(29).

5. INVESTIGATION AND DISCUSSION OF FRR MODEL WITH MULTIMEDIA QUALITY PROTECTION

To assess the adequacy of the proposed model (1)–(30) and the demonstrativeness of the obtained calculation results, we will solve this problem for a fragment of the

infocommunication network as shown in Figs. 1 and 2. Let us assume that the network under investigation consists of sixteen routers and twenty-four communication links, indicating their capacity (1/s) in the gaps of the links.

Let the packet audio k^{sp} and video k^{video} flow be transmitted between the first and sixteenth routers with the following QoE requirements: $\lambda^{k^{sp\langle req\rangle}} = 100$ 1/s, $\lambda^{k^{video\langle req\rangle}} = 300$ 1/s, $MMq^{\langle req\rangle} \geq 3.5$, $\overline{MMq}^{\langle req\rangle} \geq 3.5$ for primary (Fig. 1) and backup (Fig. 2) multipath in ICN accordingly, when some users are dissatisfied [10].

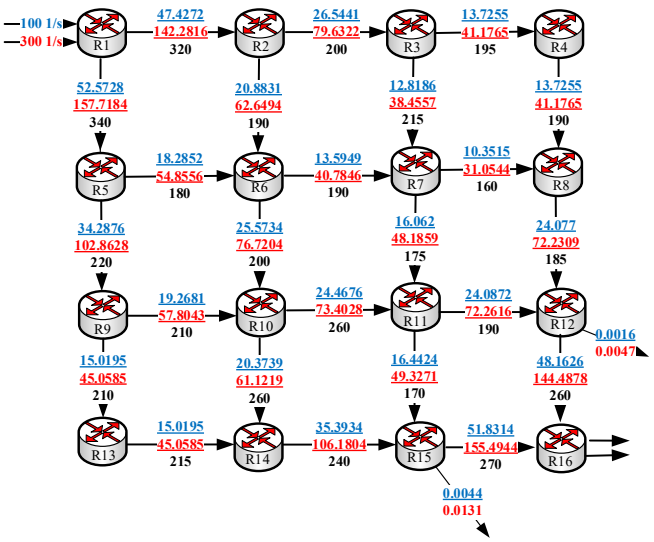

Fig. 1. The routing order of a flow of audio and video packets that is transmitted along the primary multipath.

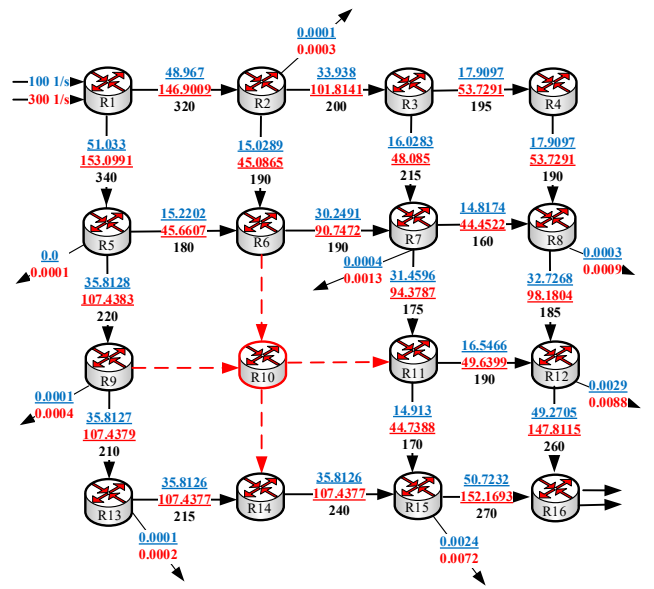

Fig. 2. The routing order of a flow of audio and video packets that is transmitted along the backup multipath.

In accordance with the presented initial data and MMq requirements for primary multipath, the solution to the fast rerouting problem has been obtained using the proposed FRR model (1)–(29), the results of which are presented in Table 1.

Table 1. Results of Solving the Problem of Providing MMq along the Primary Multipath

Link	$\varphi_{i,j}$, 1/s	QoE requirements: $\lambda^{k\,sp\langle req\rangle} = 100$ 1/s, $\lambda^{k\,video\langle req\rangle} = 300$ 1/s, $MMq^{\langle req\rangle} \geq 3.5$			
		Calculation results for the audio flow		Calculation results for the video flow	
		$\lambda_{i,j}^{k\,sp}$, 1/s	$r_{i,j}^{k\,sp}$, 1/s	$\lambda_{i,j}^{k\,video}$, 1/s	$r_{i,j}^{k\,video}$, 1/s
(1,2)	320	47.4272	0	142.2816	0
(1,5)	340	52.5728	0	157.7184	0
(2,3)	200	26.5441	0	79.6322	0
(2,6)	190	20.8831	0	62.6494	0
(3,4)	195	13.7255	0	41.1765	0
(3,7)	215	12.8186	0	38.4557	0
(4,8)	190	13.7255	0	41.1765	0
(5,6)	180	18.2852	0	54.8556	0
(5,9)	220	34.2876	0	102.8628	0
(6,7)	190	13.5949	0	4037846	0
(6,10)	200	25.5734	0	76.7204	0
(7,8)	160	10.3515	0	31.0544	0
(7,11)	175	16.062	0	48.1859	0
(8,12)	185	24.077	0	72.2309	0
(9,10)	210	19.2681	0	51.8043	0
(9,13)	210	15.0195	0	45.0585	0
(10,11)	260	24.4676	0	73.4028	0
(10,14)	260	20.3739	0	61.1219	0
(11,12)	190	24.0872	0	72.2616	0
(11,15)	170	16.4424	0	49.3271	0
(12,16)	260	48.1626	0.0016	144.4878	0.0047
(13,14)	215	15.0195	0	45.0585	0
(14,15)	240	35.3934	0	106.1804	0
(15,16)	270	51.8314	0.0044	155.4944	0.0131

The results of calculation of MMq level along the backup multipath according to the initial requirements are presented in Table 2.

Table 2. Results of Solving the Problem of Providing MMq along the Backup Multipath

Link	$\varphi_{i,j}$, 1/s	QoE requirements: $\overline{\lambda}^{k\,sp\langle req\rangle} = 100$ 1/s, $\overline{\lambda}^{k\,video\langle req\rangle} = 300$ 1/s, $\overline{MMq}^{\langle req\rangle} \geq 3.5$			
		Calculation results for the audio flow		Calculation results for the video flow	
		$\overline{\lambda}_{i,j}^{k\,sp}$, 1/s	$\overline{r}_{i,j}^{k\,sp}$, 1/s	$\overline{\lambda}_{i,j}^{k\,video}$, 1/s	$\overline{r}_{i,j}^{k\,video}$, 1/s
(1,2)	320	48.967	0	146.9009	0
(1,5)	340	51.033	0	153.0991	0
(2,3)	200	33.938	0.0001	101.8141	0.0003
(2,6)	190	15.0289	0	45.0865	0
(3,4)	195	17.9097	0	53.7291	0
(3,7)	215	16.0283	0	48.085	0
(4,8)	190	17.9097	0	53.7291	0
(5,6)	180	15.2202	0	45.6607	0
(5,9)	220	35.8128	0	107.4383	0.0001
(6,7)	190	30.2491	0	90.7472	0
(6,10)	0	0	0	0	0
(7,8)	160	14.8174	0	44.4522	0
(7,11)	175	31.4596	0.0004	94.3787	0.0013
(8,12)	185	32.7268	0.0003	98.1804	0.0009
(9,10)	0	0	0	0	0
(9,13)	210	35.8127	0.0001	107.4379	0.0004
(10,11)	0	0	0	0	0
(10,14)	0	0	0	0	0
(11,12)	190	16.5466	0	49.6399	0
(11,15)	170	14.913	0	44.7388	0
(12,16)	260	49.2705	0.0029	147.8115	0.0088
(13,14)	215	35.8126	0.0001	107.7377	0.0002
(14,15)	240	35.8126	0	107.4377	0
(15,16)	270	50.7232	0.0024	152.1693	0.0072

As a result of the calculations (see Table 1, Table 2), which quantitatively meet the requirements for ensuring the level of multimedia quality in the network along the primary multipath (9) at $MMq^{\langle req\rangle} \geq 3.5$, and along the backup multipath, the following values obtained are presented in Table 3.

Table 3. Results of Solving the Problem of Providing FRR with the Level of MMq in ICN

	Calculation results for the MMq value along the primary multipath	Calculation results for the MMq value along the backup multipath
Multimedia quality	$MMq = 3.5083$	$\overline{MMq} = 3.5004$
The transmission quality of audiovisual information for audio and video flow packets	$MM_{SV} = 3.3539$	$\overline{MM}_{SV} = 3.3530$
The degradation in quality due to delays and desynchronization of processes for transmitting audio and video flow packets	$MM_T = 3.8768$	$\overline{MM}_T = 3.8668$
The average delays of packets of audio and video flows, 1/s	$T_S = T_V = 0.059$	$\overline{T}_S = \overline{T}_V = 0.0745$
The probabilities of the total losses of packets of audio and video flows	$P^S = P^V = 0.001$	$\overline{P}^S = \overline{P}^V = 0.009$
Evaluation of MMq level [19]	Some users dissatisfied	Some users dissatisfied

Among the results of the calculations shown in Table 3, it was possible to provide a given level of multimedia quality along the primary (Table 1) and backup (Table 2) multipath. The level of multimedia quality through the backup path ($\overline{MMq} = 3.5004$) was slightly lower than the primary path ($MMq = 3.5083$). This was determined by the fact that when calculating the backup path in the network structure was without router $R10$ and incident links to it, which affected the bandwidth of the network in general. A characteristic feature of the routing solutions obtained is that the average packet delays along routes that formed a single primary (Fig. 1) or separately backup (Fig. 2) multipath were the same for both audio and video flows. This effect was positive about the value of Eq. (16) associated with the decryption of the audio and video flow packet arrivals that were transmitted within a single multimedia session.

6. CONCLUSIONS

In this paper, a tensor flow-based model of fast rerouting with protection of the multimedia quality level has been proposed. This fast rerouting model belongs to the class of flow-based models and includes the conditions for implementing a multipath routing strategy (1), the conditions for conservation of audio and video flows taking into account possible losses at the network nodes (2) and preventing overloading of links (6) both when using the primary and backup routes. At the same time, the novelty of the proposed solution is ensuring the level of multimedia quality not only along the primary route, but also along the backup one. This has been achieved by analytically calculating the QoS indicators: packet loss probabilities for audio and video flows (17), (18), as well as the average end-to-end delays (26), (28) for the same flows transmitted within the multimedia session when using primary and backup routes, respectively. Expressions (26), (28) characterizing the average end-to-end delay of audio and video flows of packets, respectively, along the primary route, as well as similar expressions for calculating this QoS indicator when using the backup route, have been obtained using the tensor research methodology. Thus, the possibility of an analytical

and interconnected calculation of end-to-end QoS indicators (25) allows controlling the impact of time desynchronization in the delivery processes of packets of audio and video flows (14)–(16) on Multimedia Quality using the primary (9) and backup (10) routes, which is very important in the practical implementation of the proposed routing model.

The research of the proposed model with multimedia quality protection has been carried out on the example of the network presented in Figs. 1 and 2. The results of the research have confirmed the adequacy of the calculated results obtained to solve the problem of fast rerouting with link/node protection. Due to the introduction of conditions (9) into the structure of the model and control over the values of the average end-to-end packet delay (26) and (28), as well as the probability of packet loss (17), (18), it was possible to provide a set level of multimedia quality along both the primary (Table 1) and the backup routes (Table 2).

REFERENCES

1. Savva, S. (2017). Fault-tolerant routing methodology for Networks-on-Chip. In *27th International Symposium on Power and Timing Modeling, Optimization and Simulation (PATMOS)*, (pp. 1–3), 25–27 September 2017, Thessaloniki, Greece. DOI:10.1109/PATMOS.2017.8106993
2. Ren, Y., Liu, L., Yin, S., Han, J., Wu, Q., & Wei, S. (2013). A Fault Tolerant NoC Architecture Using Quad-Spare Mesh Topology and Dynamic Reconfiguration. *Journal of Systems Architecture. Elsevier*, *59* (7), 482–491. DOI:10.1016/j.sysarc.2013.03.010
3. Papán, J., Segeč, P., Moravčík, M., Hrabovský, J., Mikuš, Ľ., & Uramova, J. (2017). Existing mechanisms of IP fast reroute. In *15th International Conference on Emerging eLearning Technologies and Applications (ICETA)*, (pp. 1–7), 26–27 October 2017, Stary Smokovec. DOI:10.1109/ICETA.2017.8102516
4. Seufert, M., & Tran-Gia, P. (2018). Quality of experience and access network traffic management of HTTP adaptive video streaming. *In IEEE/IFIP Network Operations and Management Symposium,* (pp. 1–8), 23–27 April 2018, Taipei. DOI:10.1109/NOMS.2018.8406136
5. Liotou, E., Tsolkas, D., & Passas, N. (2016). A roadmap on QoE metrics and models. In *23rd International Conference on Telecommunications* (ICT), (pp. 1–5), 16–18 May 2016, Thessaloniki, Greece. DOI:10.1109/ICT.2016.7500363
6. Litvinenko, A., & Aboltins, A. (2016). Selection and performance analysis of chaotic spreading sequences for DS-CDMA systems. In *Advances in Wireless and Optical Communications (RTUWO)*, (pp. 38–45), 3–4 November 2016, Riga, Latvia. DOI: 10.1109/RTUWO.2016.7821852
7. Kondratjevs, K., Kunicina, N., Patlins, A., Zabasta, A., & Galkina, A. (2016). Vehicle weight detection sensor development for data collecting in sustainable city transport system. In *57th International Scientific Conference on Power and Electrical Engineering of Riga Technical University (RTUCON)*, (pp. 1–5), 13–14 October 2016, Riga, Latvia. DOI: 10.1109/RTUCON.2016.7763136
8. Dorogovs, P., & Romanovs, A. (2015). Overview of government e-service security challenges. In *IEEE 3rd Workshop on Advances in Information, Electronic and Electrical Engineering (AIEEE),* (pp. 1–5), 13–14 Novenber 2015, Riga, Latvia. DOI: 10.1109/AIEEE.2015.7367316

9. Gasparjans, A., Terebkov, A., & Žiravecka, A. (2017) Application of Resonance Method for Examining of Piston Ring Technical Condition. In *16th International Scientific Conference "Engineering for Rural Development"*, (pp.884–891), 24–26 May, 2017, Latvia, Jelgava. DOI:10.22616/ERDev2017.16.N180
10. Hands, D.S. (2001). A basic multimedia quality model. *IEEE Transactions on Multimedia, 6* (6), 806–816. DOI: https://doi.org/10.1109/TMM.2004.837233
11. Lemeshko, O., Yeremenko, O., Yevdokymenko, M., Nevzorova, O., Snihurov, A., & Kovalenko, T. (2019). Fast reroute model with VoIP quality of experience protection. In *IEEE 3rd International Conference on Advanced Information and Communications Technologies (AICT)*, (pp. 16–21), 2–3 July 2019, Lviv, Ukraine. DOI: 10.1109/AIACT.2019.8847918.
12. Churyumov, G., Tkachov, V.M., Tokariev, V., & Diachenko, V. (2018). Method for Ensuring Survivability of Flying Ad-hoc Network Based on Structural and Functional Reconfiguration. In *XVIII International Scientific and Practical Conference "Information Technologies and Security" (ITS)*, (pp. 64–76), 27 November 2018, Ukraine.
13. Tkachov, V., & Savanevych, V. (2014). Method for transfer of data with intermediate storage. In *First International Scientific-Practical Conference Problems of Infocommunications Science and Technology*, (pp. 105–106), 14–17 October 2014, Kharkiv, Ukraine. DOI: 10.1109/INFOCOMMST.2014.6992315
14. Lemeshko, O., Yeremenko, O., Yevdokymenko, M., Hailan, A.M., Segeč, P., & Papán, J. (2019). Design of the fast reroute QoS protection scheme for bandwidth and probability of packet loss in software-defined WAN. In *15th International Conference "The Experience of Designing and Application of CAD Systems (CADSM)"*, (pp. 3/72–3/76), 26 February–2 March 2019, Polyana,Ukraine. DOI: 10.1109/CADSM.2019.8779321
15. Lemeshko, O., Yevsieieva, O., & Yevdokymenko, M. (2018). Tensor flow-based model of quality of experience routing. In *IEEE 14th International Conference on Advanced Trends in Radioelecrtronics, Telecommunications and Computer Engineering (TCSET)*, (pp. 1005–1008), 20–24 February 2018, Lviv, Ukraine. DOI: 10.1109/TCSET.2018.8336364.
16. Lemeshko, O., Yeremenko, O., & Yevdokymenko, M. (2020). Traffic Engineering Solution of Multipath Fast ReRoute with Local and Bandwidth Protection. In *Advances in Computer Science for Engineering and Education II. ICCSEEA 2019. Advances in Intelligent Systems and Computing*, (pp.113–125), 29 March 2019. Springer, Cham, vol. 938. DOI:10.1007/978-3-030-16621-2_11
17. Lemeshko, O., Yevdokymenko, M., & *Alsaleem*, N. (2018). Development of the Tensor Model of Multipath QoE-Routing in an Infocommunication Network with Providing the Required Quality Rating. *Eastern-European Journal of Enterprise Technologies, 5* 2(95), 40–46. DOI: 10.15587/1729-4061.2018.141989
18. Lin, S.C., Wang, P., & Luo, M. (2016). Control Traffic Balancing in Software Defined Networks. *Computer Networks*, *106*, 260–271.
19. Akhtar, Z., & Falk, T.H. (2017). Audio-Visual Multimedia Quality Assessment: A Comprehensive Survey. *IEEE Access., 5*, 21090–21117. DOI: 10.1109/ACCESS.2017.2750918
20. Floris, Atzori, L., & Ginesu, G. (2014). Addressing un-interoperability issues in QoE models: Is a layered modelling effective? In *IEEE International Conference on Communications Workshops (ICC),* (pp. 563–568), 10–14 June 2014, Sydney, NSW. . DOI: 10.1109/ICCW.2014.6881258
21. Rehman Laghari, K.U., & Connelly, K. (2012). Toward Total Quality of Experience: A QoE Model in a Communication Ecosystem. *IEEE Communications Magazine*, *50* (4), 58–65. DOI: 10.1109/MCOM.2012.6178834

22. Seppänen, J., Varela, M., & Sgora, A. (2014). An Autonomous QoE-driven Network Management Framework. *Journal of Visual Communication and Image Representation*, *25* (3), 565–577.
23. ITU-T G.1070. (2012). *Opinion Model for Video-Telephony Applications*.
24. Yevdokymenko, M. (2019). Routing tensor model with providing multimedia quality. In *International Scientific-Practical Conference Problems of Infocommunications. Science and Technology (PIC S&T),* (pp. 1–4), 8–11 October 2019, Kyiv, Ukraine.
25. Kron, G. (1949). *Tensor Analysis of Networks*. J. Wiley and Sons.
26. Ahmad, A., Floris, A., & Atzori, L. (2016). QoE-centric Service Delivery: A Collaborative Approach among OTTs and ISPs. *Computer Networks*, *110*, 168–179.
27. Georgopoulos, P., Elkhatib, Y., Broadbent, M., Mu, M., & Race, N. (2013). Towards network-wide QoE fairness using openflow-assisted adaptive video streaming. In *SIGCOMM Workshop on Future Human-Centric Multimedia Networking*, (pp. 15–20), 16 August 2013, Hong Kong, China.
28. Patlins, A., & Kunicina, N. (2014). The use of remote sensing technology for the passenger traffic flow dynamics study and analysis. In *Transport Means – Proceedings of the International Conference*, (pp. 63–66), 23–24 October 2014, Kaunas, Lithuania.

sciendo

LATVIAN JOURNAL OF PHYSICS
AND TECHNICAL SCIENCES
2021, N 6

DOI: 10.2478/lpts-2021-0046

THREE STAGES OF COMPOSITE SPECIMEN DESTRUCTION IN STATIC FAILURE

M. Urbaha[1]*, I. Agafonovs[2], V. Turko[3], J. Fescuks[4]

[1,2,4] Latvian Maritime Academy,
12 Flotes Str., Riga, LV-1016, LATVIA
[3] Riga Technical University,
1 Kalku Str., Riga, LV-1048, LATVIA
*e-mail: Margarita.Urbaha@latja.lv

The paper presents the results of standard specimen fracture made of anisotropic carbon fiber plastic with an epoxy matrix. Static stepwise loading of the specimen was carried out on an Instron 8801 testing machine to determine the characteristics of ductile fracture G_{1C} in the first mode in accordance with ASTM D5528.

During loading, the parameters of acoustic emission (AE) signals, such as AE impulse amplitudes and their energy were synchronously recorded. At the same time, the magnitude of the opening and the growth of the crack initiated by the artificial cut at the end of the specimen were recorded.

According to the analysis of the acoustic emission signals, three zones with different G_{1C} behaviour were identified: initial crack propagation, its stationary growth and accelerated fracture of the specimen. The zonal character of the change in the acoustic emission signals made it possible to determine the energy of the acoustic emission signals as diagnostic evidence for the onset of rapid destruction of the specimen.

The amplitude of the AE-signals in the zones, however, remained constant. Online monitoring of changes in the energy of acoustic emission signals will prevent the onset of rapid destruction of an object in places of its deformations. The paper does not aim at defining G_{1C} as usual. It presents the investigation of the fracture stages for a composite material using an acoustic emission method.

Keywords: *Acoustic emission data analysis, carbon fiber, composite specimen destruction.*

1.INTRODUCTION

The paper deals with the determination of opening Mode I interlaminar fracture toughness, $G_I c$, for continuous fiber-reinforced composite materials using the double cantilever beam (DCB) specimen. During testing, an acoustic emission (AE) method was applied to obtain experimental data. $G_I c$ calculation was performed in compliance with ASTM D5528 [1] using a method of Modified Beam Theory (MBT) (Fig. 1).

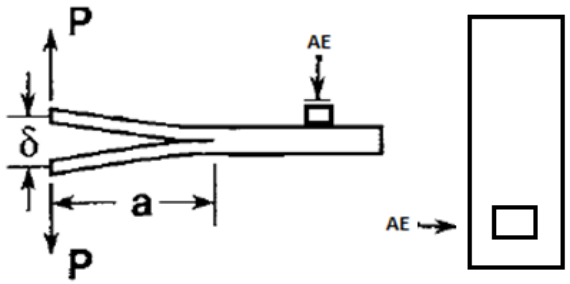

Fig. 1. Scheme of determination of G1c according to ASTM D5528.

where P – load, N; δ – crack opening, mm; b – specimen width, mm; a – crack length, mm; AE – acoustic emission gauge.

2. EXPERIMENTAL

Specimens were made of carbon fiber zero-degree orientation (see Fig. 2). On the both sides, metallic hinges have been glued to transfer load during loading. The dimensions of specimens are 200 mm x 25 mm x 3 mm. Before testing, in each specimen cleavage about 50 mm was made as crack initiator with utility knife. The Instron 8801 machine was used for specimen stepwise loading (loading-unloading). The Instron 8801 100 kN is a compact servo hydraulic fatigue testing system that meets the challenging demands of various static and dynamic testing requirements. 8801 systems provide complete testing solutions to satisfy the needs of advanced materials and component testing, and are ideally suited for fatigue testing and fracture mechanics [2]. For measurement crack length and crack opening, digital caliper was used [3]. During testing, Vallen system AMSY-6 digital multi-channel acoustic emission (AE) acquisition system was used. Vallen AMSY-6 is a fully digital multi-channel AE measurement system. A measurement channel consists of an AE sensor, preamplifier and one channel of an ASIP-2 (dual channel acoustic signal processor). Each channel combines an analogue measurement section and a digital signal processing unit. AE features, such as time of the first threshold crossing (arrival time), rise time, duration, peak amplitude, energy and counts, are extracted by the ASIP-2 [4]. According to the procedure, the calibration was performed using a standardized source of Hsu-Nielsen (Hsu-Nielsen source). In this case, the threshold value was 30.1 dB [5].

The AMSY-6 provides four types of measurement data:

- Hit data: data that are generated when the AE signal exceeds the threshold;
- Status data: data that are generated in regular time intervals;
- Parametric data: data of external parametric sensors which are measured at regular time intervals. Parametric data are stored with every hit and at user-specified time intervals;
- Waveform data: sampled AE sensor signal.

Fig. 2. General view of specimen.

3. RESULTS AND DISCUSSION

The results of loading and measurements are averaged values over three specimens (see Table 1).

Table 1. The Results of Loading and Measurements

Average load, N	Average crack opening, mm	Average crack length, mm	Average G_{1C},	Average AE Energy, J	Average amplitude, A
0	0.00	50.91	0.00	27643	69.3
48	5.83	52.07	0.27	829802	83.6
69	7.57	54.04	0.50	1835112	94.8
77	8.62	55.58	0.61	8001274	95.9
68	10.18	58.93	0.60	32349678	100.0
65	11.34	60.51	0.62	17617166	100.0
59	12.59	64.88	0.58	2101359	96.0
51	13.92	66.19	0.55	11062139	100.0
51	15.42	67.96	0.58	8762451	99.8
45	17.47	70.97	0.56	18522012	100.0
39	19.57	76.21	0.51	6130811	86.3
36	20.88	78.73	0.48	802792	92.2
31	23.93	82.68	0.46	4653842	99.1
29	27.03	87.22	0.45	6168770	100.0
26	30.46	92.14	0.44	11803327	100.0
25	32.98	95.21	0.44	4050307	86.4
12	37.77	102.50	0.33	635252	81.7
9	42.30	103.60	0.19	32199243	100.0

Energy is given in energy units (eu) and the software takes the selected gain into account, when calculating and displaying energy. Energy is calculated by squaring the digitized AE signal and integrating the results during the hit. 1 eu corresponds to $10^{-14}V^2$ sec at the sensor output [6]. Energy is processed in either the so-called true energy mode or a signal strength mode. In both modes, energy is given in energy units and the software takes the selected gain into account, when calculating and displaying energy. Energy is stored in a logarithm format with a resolution of 0.1 %.

Figure 3 shows the change in G_{IC} with loads.

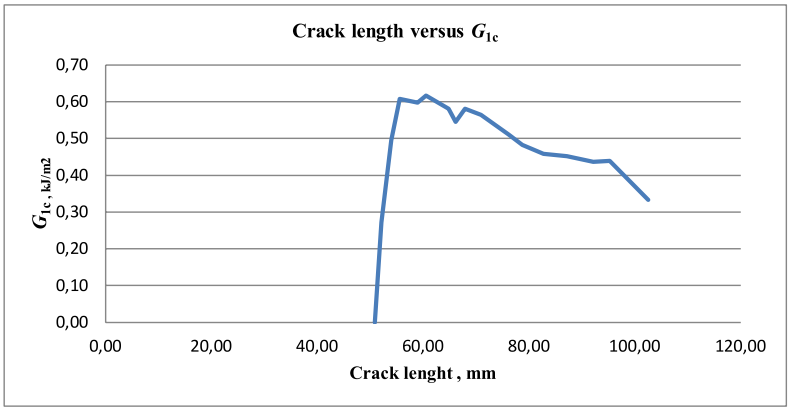

Fig. 3. The change in the fracture toughness in Mode 1 in the load.

A characteristic change in fracture toughness is observed during an increase in the load [7]. Due to a non-monotonic increase in the fracture toughness value, it is very difficult to determine the moment of termination of loading for its calculation. Figure 4 demonstrates a comparison of the change in crack opening and crack length. An increase in crack opening and crack length depends on the loading. After maximal load cracks continue increasing, but the loads decrease.

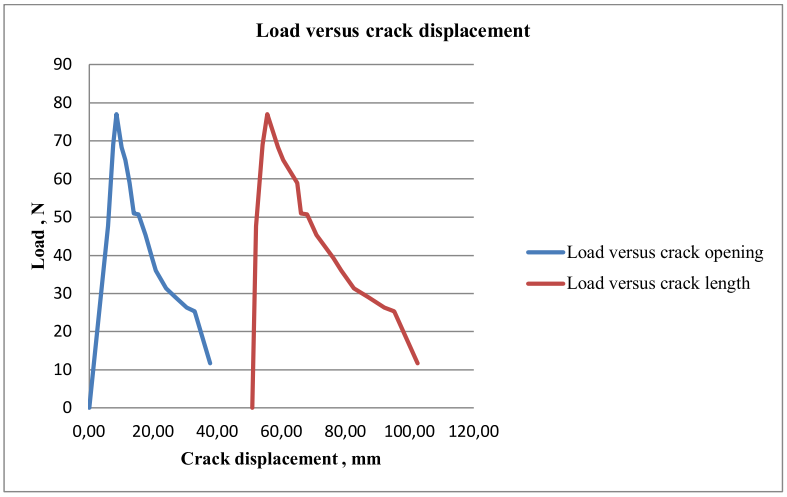

Fig. 4. The change in crack opening and crack length evolution during loading.

As the probable moment of specimen destruction cannot be predicted exactly and crack opening is difficult to measure on a real object, there is a problem related to the operation of instrumental control over the beginning of accelerated destruction of the specimen [8].

Let us consider the changes in the parameters of acoustic emission signals under loading of the specimens. The use of the acoustic emission method for full-scale bench tests of aircraft structures and/or their components shows that this method is the most effective and convenient to use for monitoring the technical state of the controlled object [9]–[13]. This integrated method allows monitoring a rather extensive area free of NDT Operator in the online regime [14]. When diagnostic signs of incipient fracture appear, it becomes possible for the Operator to periodically use other methods of instrumental control of a suspicious area, but already in specific places of destruction [15], [16].

Table 2 shows loading stages for each measurement channel.

Table 2. Three Stages of Composite Specimen Destruction

Recording parameter	Initial zone, P	Increasing zone, P	Destruction zone, P
G_{1c},	0–48 N	48–12 N	12–9 N
Crack opening, mm			
Crack length, mm			
AE energy, eu			
AE amplitude, A			

Figure 5 shows changes in the AE energy and amplitude, and Fig. 6 demonstrates changes in the AE energy and G_{1C}.

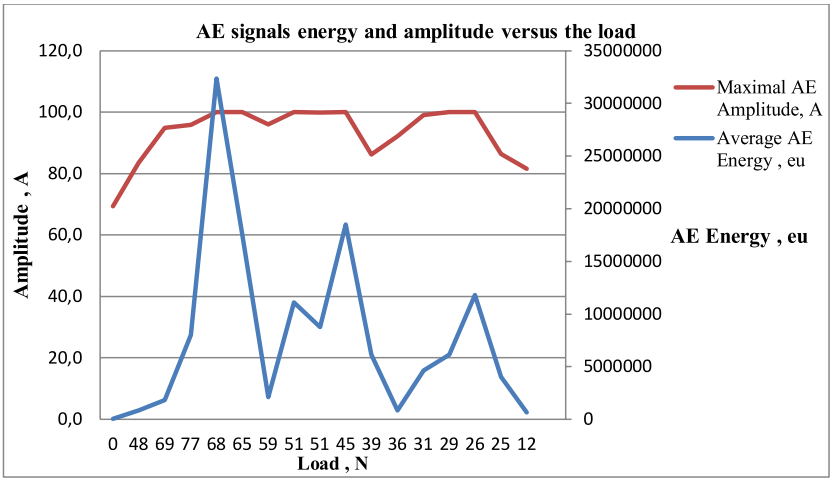

Fig. 5. Changes in AE energy and amplitude versus the load.

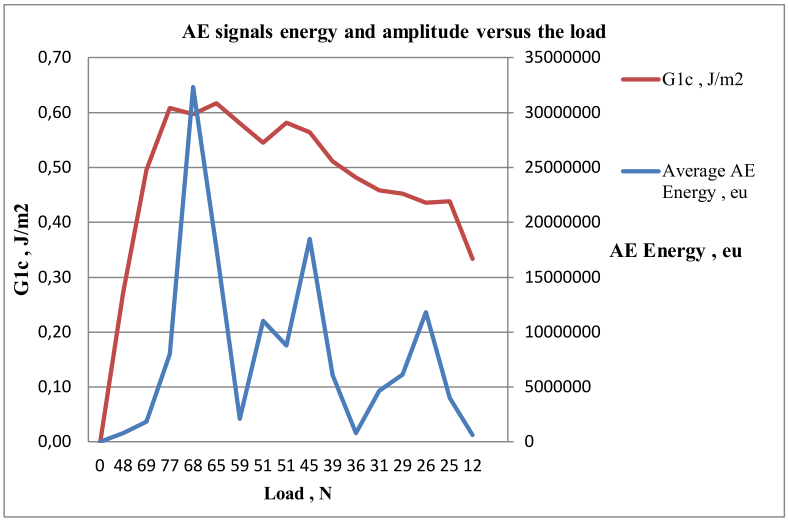

Fig. 6. Changes in AE energy depending on the G_{1C}.

Figures 5 and 6 clearly show three zones of successive destruction of the composite material of the specimens. Thus, it is possible to objectively record the moment of the onset of accelerated destruction of the specimen. The most pronounced criterion here is the change in the energy of acoustic emission signals, while the maximum amplitude of the AE signals does not so characteristically record this moment.

4. CONCLUSIONS

The investigation of the fracture toughness of Mode 1 allows observing the moment of decreased loading. However, this moment is determined subjectively, and then impossibility of withstanding the load or its fall occurs. The research has shown that the nature of the sequential fracture of the composite material of standard specimen with a longitudinal cut is characterised by three zones: initial (from the moment the crack starts to move in the cut), stationary, and accelerated.

On-line acoustic emission monitoring of specimen fracture made it possible to objectively observe these zones and showed that the main diagnostic criterion was the energy of the acoustic emission signal. Thus, it will be possible to use this method in real designs subjected to deformations. The use of the acoustic emission method allows predicting the start and accelerated destruction of the weak elements. The composite products and structures during their deformations give objective information to Health and Usage Monitoring Systems.

ACKNOWLEDGEMENTS

The research has been supported by the European Regional Development Fund within Measure 1.1.1.2 “Aid to Post-Doctoral Research” of the Specific Aid Objective “To increase the research and innovative capacity of scientific institutions of

Latvia and the ability to attract external financing, investing in human resources and infrastructure" of the Operational Programme "Growth and Employment" (No. 1.1.1.2/VIAA/1/16/104 Structural Health Monitoring System for Inflight Monitoring (FLY SAFE System).

REFERENCES

1. Standard Test Method for Mode I Interlaminar Fracture Toughness of Unidirectional Fiber-Reinforced Polymer Matrix Composites. (n.d.) Available at https://www.astm.org/Standards/D5528
2. 8801 (100kN) Fatigue Testing Systems. (n.d.). Available at https://www.instron.us/products/testing-systems/dynamic-and-fatigue-systems/servohydraulic-fatigue/8801-floor-model
3. Lingelli, A. F. (Ed.) (2009). Fatigue Crack Growth. Mechanics, Behaviour and Prediction. New York: Nova Science Publishers Ins.
4. Multi-Channel Systems. (n.d.). Available at https://www.vallen.de/products/multi-channel-systems/
5. Hsu-Nielsen Source. (n.d.). Available at https://www.ndt.net/article/az/ae/hsunielsensource.htm
6. AMSY-5 System Description. (n.d.). Available at https://www.vallen.de/zdownload/pdf/y5sd0911.pdf
7. Urbaha, M., Turko, V., Agafonovs, I., & Sorokins, A. (2020). Experimental Evaluation of Static and Fatigue Strength of Aluminium-Based Structural Metallic Alloys. *Engineering for Rural Development*, *19*, 487–493.
8. P.E.Mix Introduction to Non-destructive Testing, training guide (2nd ed.). (2005). New Jersey: John Wiley & Sons, Inc.
9. Urbaha, M., Carjova, K., Nagaraj, P., & Turko, V. (2018). Requirements for helicopter's planer construction fatigue testing. In *Transport Means – Proceedings of the International Conference*, (pp. 1268–1270), 3–5 October 2018, Trakai, Lithuania.
10. Urbahs, A., Banovs, M., Turko, V., Urbaha, M., Nedelko, D., & Lebedevs, I. (2019). Research into the features of service damage in the composite material of helicopter rotor blades. In *Transport Means – Proceedings of the International Conference*, (pp. 466–469), 2–4 October 2019, Kaunas, Lithuania.
11. Гузь А.Н., Хорошун Л.П., Ванин Г.А., Бабич И.Ю., Каминский А.А., Шульга Н.А., Маслов Б.П., & Скиченко А.В. (1982). Механика композитных материалов и элементов конструкций. Киев: Наук. думка.
12. Finlayson, R.D., Friesel, M., Carlos, M., Cole, P., & Lenein, J.C. (2001). Health monitoring of aerospace structures with acoustic emission and acousto-ultrasonics. In *15th World Conference on NDT*, 15–21 October, 2000, Rome, Italy. INSIGHT,*43* (3).
13. Фейгенбаум Ю.М., Дубинский С.В., Божевалов Д.Г., Соколов Ю.С., Метелкин Е.С., Миколайчук Ю.А., & Шапкин В.С. (2018). Обеспечение прочности композиционных авиационных конструкций с учетом случайных эксплуатационных ударных воздействий. *М.:* Техносфера.
14. Prostaks, J., & Urbaha, M. (2019). Evaluating Accuracy of Fault Localization when Monitoring Condition of Large Structures by Acoustic Method. *Engineering for Rural Development*, *18*, 1280–1286.
15. Nedelko, D., Urbahs, A., Turko, V., Urbaha, M., Carjova, K., & Nagaraj, P. (2019). Assessment of the Limits of Signs of Health and Usage Monitoring System for Helicopter Transmission. *Procedia Computer Science, 149*, 252–257.
16. Turko, V. (2015). *Principle of Local Zones Applied to Fatigue Prone Large-scale Designs.* Lambert Academic Publishing. DOI: 10.22616/ERDev2020.19.TF111